



Ensemble simulation of the Last Glacial Maximum marine biogeochemistry and atmospheric pCO_2 drawdown due to the soft-tissue biological carbon pump

Chia-Te Chien^{1,2}, Markus Pahlow¹, Christopher J. Somes¹, Markus Schartau¹, and Andreas Oschlies¹

¹GEOMAR Helmholtz Centre for Ocean Research Kiel, Kiel, Germany

Correspondence: Chia-Te Chien (cchien308@ntu.edu.tw)

Abstract.

During the Last Glacial Maximum (LGM), atmospheric pCO₂ was approximately 90 ppm lower than in the pre-industrial era. Several hypotheses have been proposed to explain this difference, including changes in nutrient supply, increased iron input to the ocean, and variations in overturning circulation strength driven by differences in wind stress and atmospheric moisture diffusivity. Current modeling approaches that simulate LGM marine biogeochemistry typically use parameter sets calibrated under pre-industrial conditions, assuming that these parameter values are generic and independent of environmental conditions. This could introduce uncertainty due to the imperfect knowledge of the values that should be assigned to the parameters for the LGM environment. The extent to which this uncertainty affects the simulated LGM marine biogeochemistry remains unclear. In this study, we employ an optimality-based variable stoichiometry plankton ecosystem model coupled with a 3D Earth system model to simulate LGM conditions. We conduct sensitivity analyses with 24 combinations of marine biogeochemical (reduced benthic denitrification rate, decreased sedimentary iron input, a higher PO₄³⁻ inventory, and increased atmospheric iron deposition) and physical boundary conditions (changes in wind stress pattern and increased meridional moisture diffusivity over the Southern Ocean). For each combination, we perform 20 simulations using 20 biogeochemical parameter sets selected out of 600—each calibrated against present-day observations and representing pre-industrial biogeochemistry about equally well—resulting in a total of 480 simulations. Our results show that changes in iron input exert the most profound influence on marine biogeochemistry, but reduced sedimentary input counteracts the contribution of enhanced atmospheric deposition to pCO2 drawdown. Changes in macro-nutrient alone have limited effects, owing to co-limitation effects and the variable stoichiometry in our model. The impact of physical conditions on biogeochemical tracers varies, depending on the specific biogeochemical settings. We found that the changes in carbon to nutrient ratios in particulate organic matter are positively correlated with the changes in Fe supply, and could amplify the effect of Fe availability on changes in the atmospheric pCO₂. Compared to pre-industrial reference conditions, atmospheric pCO₂ under full LGM conditions decreases by 36 to 58 ppm across the 20 simulations. The difference between the maximum and minimum glacial pCO₂ decreases amounts to 50% of the 43 ppm average decrease. These findings highlight that although the 20 parameter sets similarly reproduce pre-industrial marine biogeochemistry, significant variance remains in the marine biogeochemical and atmospheric pCO₂ responses to LGM forcings.

²Institute of Oceanography, National Taiwan University, Taipei, Taiwan



40



1 Introduction

The last glacial maximum (LGM) was characterised by substantially lower atmospheric pCO₂, making it an important case study for understanding the mechanisms influencing changes in pCO₂, with implications for future climate projections. A robust quantitative understanding of the reduced atmospheric CO₂ is still lacking, and several hypotheses have been proposed to explain the lower atmospheric pCO₂ during the LGM. Those include lower sea surface temperatures and higher solubility of CO₂, partly counteracted by reduced ocean volume and increased salinity, a higher global nitrate inventory due to reduced benthic denitrification (McElroy, 1983), and a higher global phosphate inventory driven by enhanced terrestrial erosion (Broecker, 1982; Wallmann, 2010; Wallmann et al., 2016), both associated with sea-level retreat. Other factors include changes in the AMOC (Atlantic Meridional Overturning Circulation) (Muglia and Schmittner, 2015), atmospheric moisture diffusivity (Sigman et al., 2007), and enhanced iron (Fe) input to the ocean (Martin, 1990; Martínez-García et al., 2014). Iron is a critical micro-nutrient for marine phytoplankton, particularly in high-nutrient, low-chlorophyll (HNLC) regions, where its scarcity limits productivity (Martin et al., 1987). Two major sources of Fe to the ocean are atmospheric dust deposition and sedimentary inputs. While atmospheric deposition has long been recognised as a major source of Fe, recent studies have shown that sedimentary inputs could have a much larger impact on the Fe cycle in the global ocean (Tagliabue et al., 2016; Somes et al., 2021).

Model simulations are suitable tools for studying the effects of these factors on marine biogeochemistry and their potential contribution to reduced pCO₂ during the LGM. Models that have been applied to study the LGM range from simple box model approaches (Broecker, 1982; Sarmiento and Toggweiler, 1984) to 3D Earth system models that consider ocean circulation and marine biogeochemical cycles (Bopp et al., 2003; Brovkin et al., 2007; Tagliabue et al., 2009; Somes et al., 2017; Kemppinen et al., 2019; Ödalen et al., 2020; Matsumoto et al., 2020a; Kageyama et al., 2021). The biogeochemical components of these Earth system models contain various representations of marine ecosystems, transport and sinking of particles, and cycling of macro- and micro-nutrients.

The calibration of poorly known parameters is an important part of setting up reliable biogeochemical models. In principle, calibration efforts look for a set of optimal parameter estimates that minimises a metric that quantifies the data-model misfit, such as the root mean square error. Some challenges exist in the optimisation process, particularly for Earth system models that often have to cope with sparse data availability with uneven spatial and temporal distribution (Schartau et al., 2017). Also, the computational cost for spinning up Earth system models is often high, particularly for those with higher functional complexity and higher spatial resolution. In the case of high computational costs, the number of parameter sets for which model solutions can be evaluated is limited and for this reason 'optimal' parameters are often chosen pragmatically (Séférian et al., 2016). Apart from the number of possible model runs, the choice of an appropriate metric is also crucial. This choice depends objectively on the available data considered, but it is also subjective with regard to the error model employed (Jolliff et al., 2009; Schartau et al., 2017; Kriest et al., 2020). Calibration becomes particularly challenging when it comes to simulating the LGM: Data-model misfits are usually evaluated for pre-industrial or present-day conditions. To what extent a parameter set calibrated against pre-industrial or present-day observations could similarly well represent the LGM is as yet unknown.





Here we employ an optimality-based variable stoichiometry plankton ecosystem model (OPEM) coupled to the University 60 of Victoria (UVic) Earth system model of intermediate complexity (UVic-OPEM) to simulate LGM marine biogeochemistry and atmospheric pCO₂. The model is feathered with variable stoichiometry of particulate organic matter (POM), and it resolves major biogeochemical processes in today's ocean relatively well (Pahlow et al., 2020; Chien et al., 2020; Li et al., 2024). In addition, by resolving elemental stoichiometry in UVic-OPEM, it is possible to investigate how elemental ratios of particulate organic matter may have varied during the LGM, and how those differences affect the changes in the atmospheric pCO₂. We conduct sensitivity analyses with 24 combinations of LGM boundary conditions (Table 2), namely biogeochemical (reduced benthic denitrification rate, decreased sedimentary iron input, a higher PO_4^{3-} level, and increased atmospheric iron deposition) and physical (changes in wind stress pattern and increased meridional moisture diffusivity over the Southern Ocean, Muglia and Schmittner, 2015; Sigman et al., 2007). For each combination, the subset of 20 of the 600 parameter sets was considered that exhibit the best model agreement with the observations, resulting in a total of 480 simulations. The objective of this study is to examine the potential uncertainty in LGM simulations due to the typically employed selection of one specific parameter set calibrated for pre-industrial-climate boundary conditions. We also investigate the effects of variable stoichiometry of particulate organic matter (POM) along with different biogeochemical and physical boundary conditions, on atmospheric pCO₂ and marine biogeochemistry during the LGM. We are particularly interested in identifying uncertainties that might play a role in estimating pCO₂ changes in the LGM, as these are likely to be related to the very biogeochemical mechanisms that are also relevant for assessing some ocean-based carbon dioxide removal (CDR) strategies. Our results may provide insights not only regarding the interpretation of past pCO₂ variations, but also into the effectiveness of some potential CDR approaches.

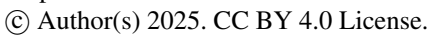
2 Materials and Methods

2.1 The UVic-OPEM Earth system model

The Optimality-based Plankton Ecosystem Model was originally implemented in UVic2.9 (Chien et al., 2020; Pahlow et al., 2020), which has since been updated to UVic2.10 (Mengis et al., 2020) for this study. In the current version, we also apply the temperature-independent mortality that has been used for ordinary phytoplankton to diazotrophs. This modification reduces nitrogen fixation in the Arctic region, where it was considered too high in Chien et al. (2020), but it has only a marginal effect on the global nitrogen distribution and fluxes.

85 2.2 Model calibration and selection of the best 20 parameter sets

We constructed 600 combinations of values assigned to 19 model parameters, including detritus remineralisation rate, the linear increase of sinking velocity with depth, and 17 parameters related to plankton physiology (Table 1). The leakage (implicit remineralisation of organic matter by bacteria) and mortality terms for non-N₂-fixing ordinary phytoplankton and diazotrophs are assumed identical to reduce the number of possible parameter combinations. The respective 600 simulations were restarted







from a previously-calibrated simulation (Chien et al., 2023) and spun up with a prescribed pre-industrial atmospheric pCO₂ of 284.3 ppm for over 10,000 years.

Table 1. Parameter names, variational ranges, the parameter set that yields the lowest cost, the lowest 20 cost parameter sets, units and descriptions. Note that ordinary phytoplankton and diazotrophs share the same temperature dependent leakage rate and temperature independent mortality rate.

Symbol	Range	Lowest	Lowest 20	Units Definition		
		cost	costs range			
$A_{0, \mathrm{ phy}}$	100-400	254.3	113.6–391.5	$m^3 (mol C)^{-1} d^{-1}$	phytoplankton potential nutrient affinity	
$A_{0,\mathrm{dia}}$	50-300	115.9	72.4–264.8	$m^3 \left(mol C \right)^{-1} d^{-1}$	diazotroph potential nutrient affinity	
$lpha_{ extsf{phy}}$	0.3-0.6	0.48	0.36-0.60	$m^2 W^{-1} (mol C) gChl^{-1} d^{-1}$	phytoplankton potential light affinity	
$lpha_{ m dia}$	0.6-1.1	0.73	0.61-1.02	$m^2 W^{-1} (mol C) gChl^{-1} d^{-1}$	diazotroph potential light affinity	
$Q_{0,\mathrm{phy}}^{\mathrm{N}}$	0.045-0.065	0.061	0.048-0.064	$\operatorname{mol}\left(\operatorname{mol} C\right)^{-1}$	phytoplankton subsistence N quota	
$Q_{0,\mathrm{dia}}^{\mathrm{N}}$	0.11-0.14	0.114	0.112-0.138	$\operatorname{mol}\left(\operatorname{mol} C\right)^{-1}$	diazotroph subsistence N quota	
$Q_{0,\mathrm{phy}}^{\mathrm{P}}$	1.4-2.3	1.97	1.46-2.28	$\operatorname{mmol} \left(\operatorname{mol} C\right)^{-1}$	phytoplankton subsistence P quota	
$Q_{0,\mathrm{dia}}^{\mathrm{P}}$	2-3.5	2.54	2.06-3.30	$\operatorname{mmol} \left(\operatorname{mol} C\right)^{-1}$	diazotroph subsistence P quota	
$k_{ m Fe,\ phy}$	0.02-0.08	0.031	0.021-0.076	$\mu \mathrm{mol}\mathrm{m}^{-3}$	phytoplankton half-saturation constant for Fe	
$k_{ m Fe,dia}$	0.10-0.16	0.11	0.10-0.15	$\mu \mathrm{mol}\mathrm{m}^{-3}$	diazotroph half-saturation constant for Fe	
$g_{ m max}$	1–1.5	1.24	1.03-1.43	d^{-1}	zooplankton maximum specific ingestion rate	
$\phi_{ m phy}$	90-300	174	119–226	$m^3 (mol C)^{-1}$	capture coefficient of phytoplankton	
$\phi_{ m dia}$	80-300	155	117–206	$m^3 (mol C)^{-1}$	capture coefficient of diazotrophs	
$\phi_{ m det}$	20-130	62	30–92	$m^3 \left(\text{mol C} \right)^{-1}$	capture coefficient of detritus	
$\phi_{ m zoo}$	45–250	175	80–175	$m^3 \left(\text{mol C} \right)^{-1}$	capture coefficient of zooplankton	
$M_{0,\mathrm{phy}}=M_{0,\mathrm{dia}}$	0.01-0.04	0.013	0.012-0.037	d^{-1}	temperature-independent mortality	
$\lambda_{0,\mathrm{phy}}=\lambda_{0,\mathrm{dia}}$	0.01-0.03	0.011	0.010-0.026	d^{-1}	temperature-dependent leakage	
$ u_{ m det}$	0.05-0.08	0.072	0.052-0.078	d^{-1}	remineralisation rate at 0 $^{\circ}$ C	
w_{dd}	0.04-0.07	0.064	0.042-0.066	d^{-1}	linear increase in sinking speed with depth	

We adopt a likelihood-based cost function for evaluating the biogeochemical model performance (Equations 4-9 in Chien et al., 2020). Our cost function considers mismatches in means, and spatial and temporal variabilities of PO_4^{3-} , excess nitrate with respect to phosphate (N* = $NO_3^- - 16 \cdot PO_4^{3-} + 2.9$ mmol m⁻³, Gruber and Sarmiento, 1997; Mills et al., 2015), and modified apparent oxygen utilisation (AOU* = $AOU - 2 \cdot PO_4^{3-}$), which eliminates the covariation between AOU and PO_4^{3-} , in 17 biomes (Fay and McKinley, 2014). Interestingly, most of the best-20 ranges cover about 80% of the total ranges, except for the four ϕ s, where the range is 'only' about 40–60%. This indicates that parameter values are relatively poorly constrained by currently available observations. The 20 best parameter sets (with the lowest cost function values) are employed for analysing model behaviour under pre-industrial (PI) and last-glacial-maximum (LGM) conditions.



100

105

110

125

130



2.3 Boundary conditions

We set-up a generic LGM configuration with LGM-specific orbital parameters of the Earth. Besides the different orbital parameters, LGM conditions likely also deviated from the pre-industrial era by a higher moisture diffusivity over the Southern Ocean and a different wind pattern, which we adopt from Somes et al. (2017) and Muglia and Schmittner (2015). In addition, we configure a 120 m lower sea level compared to PI conditions for the changes in biogeochemical fluxes (ocean bathymetry and volume remains the same as in the PI), those including reduced benthic denitrification (Somes et al., 2017), reduced sedimentary input of Fe (Tagliabue et al., 2010; Muglia et al., 2017), and a 15% increase in the PO₄³⁻ inventory (Wallmann et al., 2016). We also include a higher LGM Fe deposition, which was obtained from the LGM dust deposition estimate of Albani et al. (2014, their case C4fn-lgm). Applying a constant iron content of 3.5% and 1% solubility of deposited Fe (Kobayashi et al., 2021; Saini et al., 2023) yields an annual Fe deposition of 6.1 Gmol Fe yr⁻¹, which is about four times the pre-industrial flux (Fig. 1).

2.4 Experiment setup

We define four sets of physical and six sets of biogeochemical model configurations, two of which represent pre-industrial climate conditions, PIctl (physical) and PIallbgc (biogeochemical), and the others are different combinations of our generic LGM configuration with PI and LGM boundary conditions (Table 2): LGMatmctl and LGMallbgc refer to the full set of physical and biogeochemical LGM boundary conditions, LGMatmws has PI moisture diffusivity and LGM winds, LGMatmpi has PI moisture diffusivity and winds, and LGMFedep, LGMFesed, LGMPO₄ and LGMbdeni combine PI biogeochemical boundary conditions with one of LGM Fe deposition, Fe sedimentary release, PO₄³⁻ inventory, and benthic denitrification, respectively. These result in a total of 24 (4 physical x 6 biogeochemical) combinations of different physical and biogeochemical boundary conditions. For example, PIctl-LGMallbgc stands for simulations with pre-industrial physics and full LGM biogeochemistry (Table 2). With each of the 24 conditions, we restarted the 20 simulations with the 20 best parameter sets from the calibration stage. The spin-up were performed with fix the radiative forcing for all simulations corresponding to the respective pCO₂ (284.3 ppm for PI and 190 ppm for LGM), but let the atmospheric pCO₂ evolve freely. This physically and biogeochemically coupled but radiatively uncoupled configuration allows us to analyse the effects of different boundary conditions on pCO₂. We can also evaluate the response of terrestrial carbon in addition to the carbon exchange between the ocean and the atmosphere. All simulations were spun-up for over 10,000 years for the respective pre-industrial or glacial boundary conditions, until the marine biogeochemistry approaches a steady-state. We use the results from the last year of the spin-ups for our analysis. To evaluate whether different physical, biogeochemical, or both conditions result in ensembles which are significantly different from the 20 simulations in PIctl, PIallbgc, or PIctl-PIallbgc, we calculate their p-values for each tracer evaluated with Student's t-Test in R package "Stats". To understand if changes in individual parameters significantly influence the changes in atmospheric pCO₂ from PIctl-PIallbgc to LGMatmctl-LGMallbgc, we obtain p-values using the lm (Fitting Linear Models function) in R package "Stats".





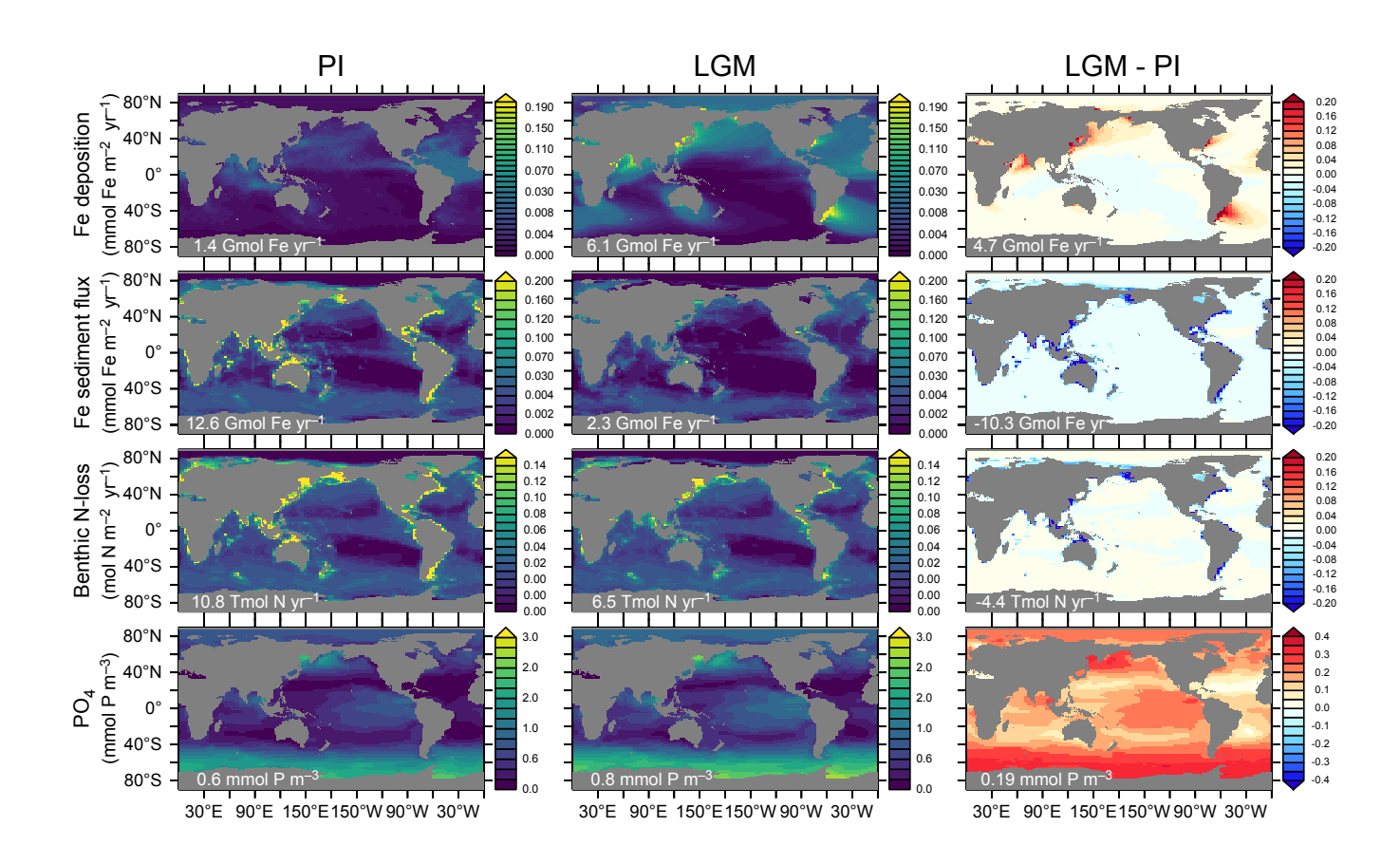


Figure 1. Fe deposition and sedimentary fluxes, benthic denitrification (benthic N-loss), and surface PO_4^{3-} in the PIallbgc and LGM biogeochemical configurations and their differences. PI results are the means of 20 simulations in PIctl-PIallbgc, and LGM Fe deposition, Fe sediment flux, benthic denitrification, and surface PO_4^{3-} are from PIctl-LGMFedep, PIctl-LGMFesed, PIctl-LGMbdeni, and PIctl-LGMPO₄ simulation means. Values on the bottom left of each panel indicate the global annual Fe and N fluxes or PO_4^{3-} concentration.





Table 2. Boundary conditions applied in the ensemble simulations for our (A) physical and (B) biogeochemical configurations .

LGMPO₄

LGMbdeni

(A)			
Physical configuration	Moisture diffusivity*	Wind stress [†]	
PIctl	PI	PI	
LGMatmctl	LGM	LGM	
LGMatmws	PI	LGM	
LGMatmpi	PI	PI	

^{*50%} lower LGM moisture diffusivity over the Southern Ocean in LGM

(B)				
Biogeochemical configuration	Fe deposition*	Fe sedimentary release [†]	PO ₄ ³⁻ inventory [§]	Benthic denitrification [‡]
PIallbgc	PI	PI	PI	PI
LGMallbgc	LGM	LGM	LGM	LGM
LGMFedep	LGM	PI	PI	PI
LGMFesed	PI	LGM	PI	PI

PΙ

PΙ

LGM

PΙ

PΙ

LGM

PΙ

PΙ

3 Results

140

3.1 Model-data misfit costs of all 600 and the selected 20 parameter sets

The 600 parameter sets yield a wide range of model-data misfit costs ranging from 1.5×10^7 to 1.4×10^9 (Fig. 2). When the initial 600 pre-industrial simulations are ordered according to increasing cost, the 600 cost values overall show an approximately exponential increase from the low to the high end, with around 8 simulations on both ends deviating from the trend. The 20 simulations with the lowest costs comprise 3.3 % of all simulations, and the 20th lowest cost value is 2.0×10^7 , which is about 1.3-fold higher than the lowest.

Globally-averaged vertical profiles of NO₃⁻, PO₄³⁻, O₂, and dissolved inorganic carbon (DIC) in the 20 simulations of PIctl-PIallbgc are compared with observational data from the World Ocean Atlas 2013 (WOA 2013, Garcia et al., 2013a, b) and GLODAPv2 (Key et al., 2015; Lauvset et al., 2016), as well as the original UVic results (Mengis et al., 2020) in Fig. 3. Among the 20 best simulations, NO₃⁻ in the upper 500 m of the model is slightly lower than in WOA 2013 but higher than the original UVic. In the deep ocean (below 2500 m), simulated NO₃⁻ concentrations are generally higher than WOA 2013. The globally-averaged concentrations range from 29.4 to 33.3 mmol m⁻³ in the model, with an average of 31.1 mmol m⁻³, which is close to 31.0 mmol m⁻³ in WOA 2013. PO₄³⁻ concentrations are slightly lower in the upper ocean but higher in the deep ocean than WOA 2013. Our 20 O₂ profiles scatter around the WOA 2013 profile and are lower and closer to the observations than the original UVic simulation documented in Mengis et al. (2020). The globally-averaged concentrations range from 165 mmol m⁻³ to 196 mmol m⁻³, with an average of 179 mmol m⁻³, which is 3 mmol m⁻³ or 1.7 % higher than WOA 2013. The DIC profiles are higher than in the original UVic and closer to the GLODAPv2 data. The globally-averaged

[†]LGM wind pattern from Somes et al. (2017); Muglia and Schmittner (2015)

^{*~4} times higher during LGM

 $^{^{\}dagger}\sim$ 5 times lower during LGM

^{§ ∼15%} higher during LGM

[‡]∼40% lower during LGM





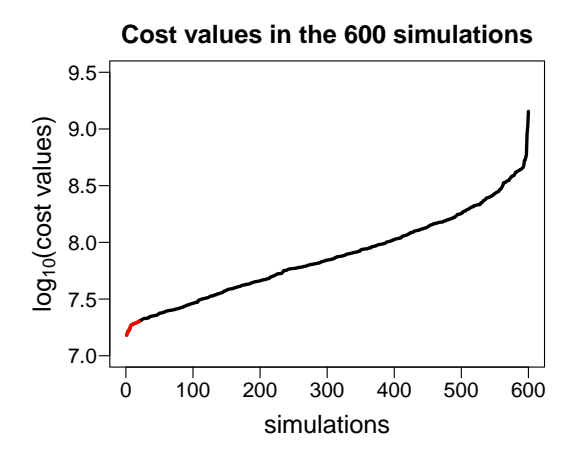


Figure 2. Cost values among all 600 simulations used for calibrating UVic-OPEM ordered from low to high. The red part denotes the 20 simulations with the lowest costs.

50 concentrations range from 2294 to $2325~\mathrm{mmol\,m^{-3}}$, with an average of $2308~\mathrm{mmol\,m^{-3}}$, which is $3~\mathrm{mmol\,m^{-3}}$ or 0.1~% higher than GLODAPv2 .

Simulated latitudinal patterns of carbon to nitrogen and carbon to phosphorus ratios in particulate organic matter (pC:N and pC:P, respectively) are also compared with observational data (Tanioka et al., 2022). Overall, the modeled ratios show good agreement with observations (Fig. 4), although both the observational data and model results exhibit substantial variability. Modeled pC:N is slightly underestimated at high latitudes (> 40 °), and overestimated at low latitudes, while pC:P in general is well reproduced across latitudes.

3.2 Effects of different physical and biogeochemical conditions

We first compare the simulations with LGM and PI physics, each combined with PI biogeochemistry (PIallbgc) to assess the glacial-interglacial changes in global temperature and the Atlantic Meridional Overturning Circulation (AMOC). We then evaluate the effects of different biogeochemical and physical conditions on marine biogeochemical inventories and atmospheric pCO₂.

3.2.1 Global temperature and ocean circulation

160

The simulated global surface air temperature in LGMatmctl-PIallbgc is 4.3° C lower than in PIctl-PIallbgc. In the ocean, the different physical boundary conditions result in distinct thermohaline circulation patterns (Fig. 5). The strength and depth of the maximum value of the AMOC in PIctl-PIallbgc at 26.5° N is 17.82 ± 0.04 Sv at 1100m, which agrees well with the observational value from the RAPID array of 17.2 ± 0.9 Sv at the same depth (McCarthy et al., 2015).

The LGM wind stress intensifies and deepens the AMOC, while the reduced moisture diffusivity across the Southern Ocean makes it weaker and shallower (Somes et al., 2017). The strength and depth of maximum AMOC at 26.5°N in LGMatmctl-



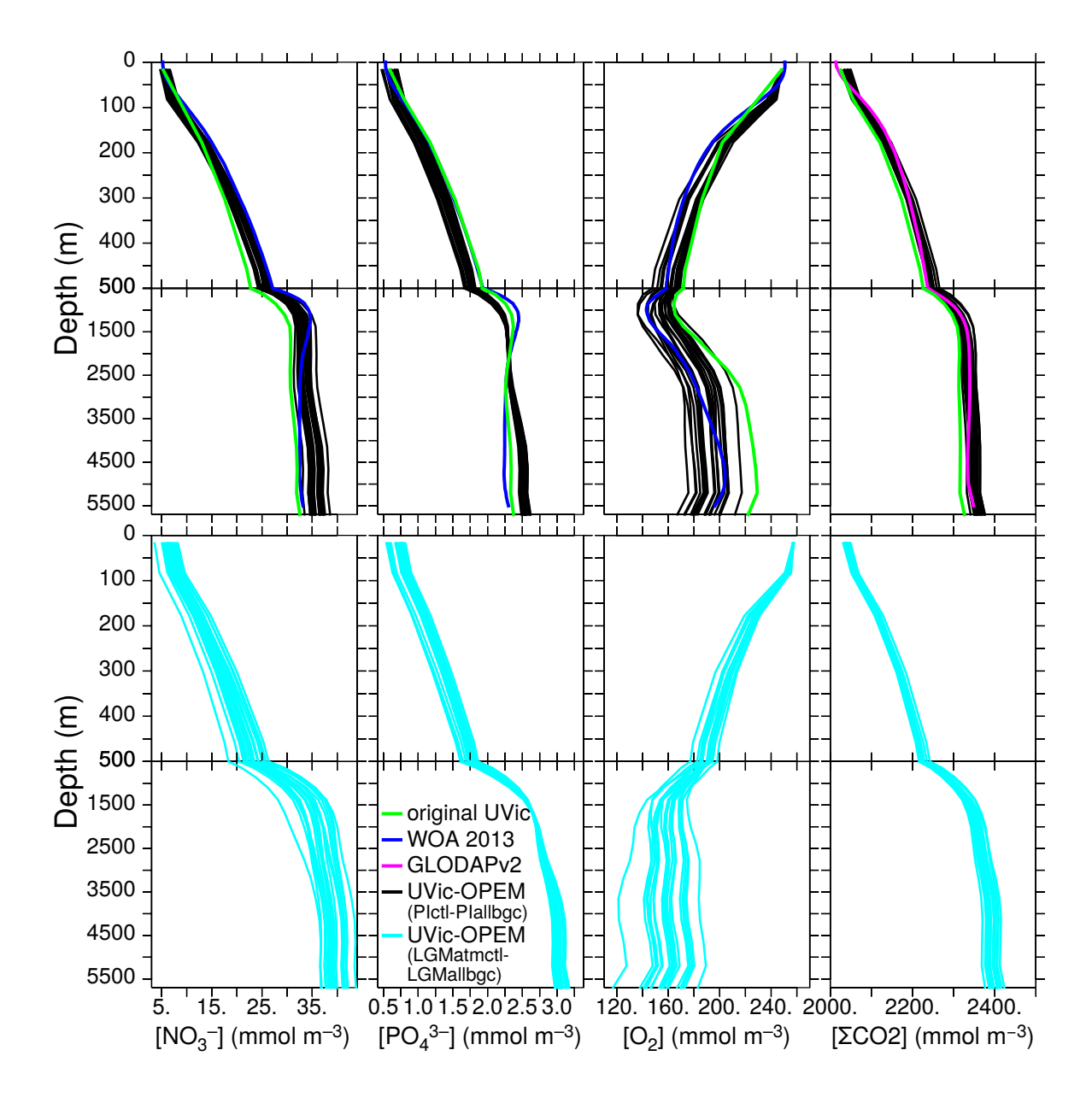


Figure 3. Globally-averaged vertical profiles of NO_3^- , PO_4^{3-} , O_2 , and DIC (ΣCO_2) concentrations. NO_3^- , PO_4^{3-} , and O_2 are considered in the cost function. Black lines are results from the 20 PIctl-PIallbgc simulations, and green lines indicate model results from the original UVic (UVic 2.10, Mengis et al., 2020). Blue and purple lines represent NO_3^- , PO_4^{3-} , and O_2 observational data from the World Ocean Atlas 2013 (WOA 2013, Garcia et al., 2013a, b) and ΣCO_2 data from GLODAPv2 (Key et al., 2015; Lauvset et al., 2016), respectively. Light blue lines in the bottom panels show results from the LGMatmctl-LGMallbgc simulations.



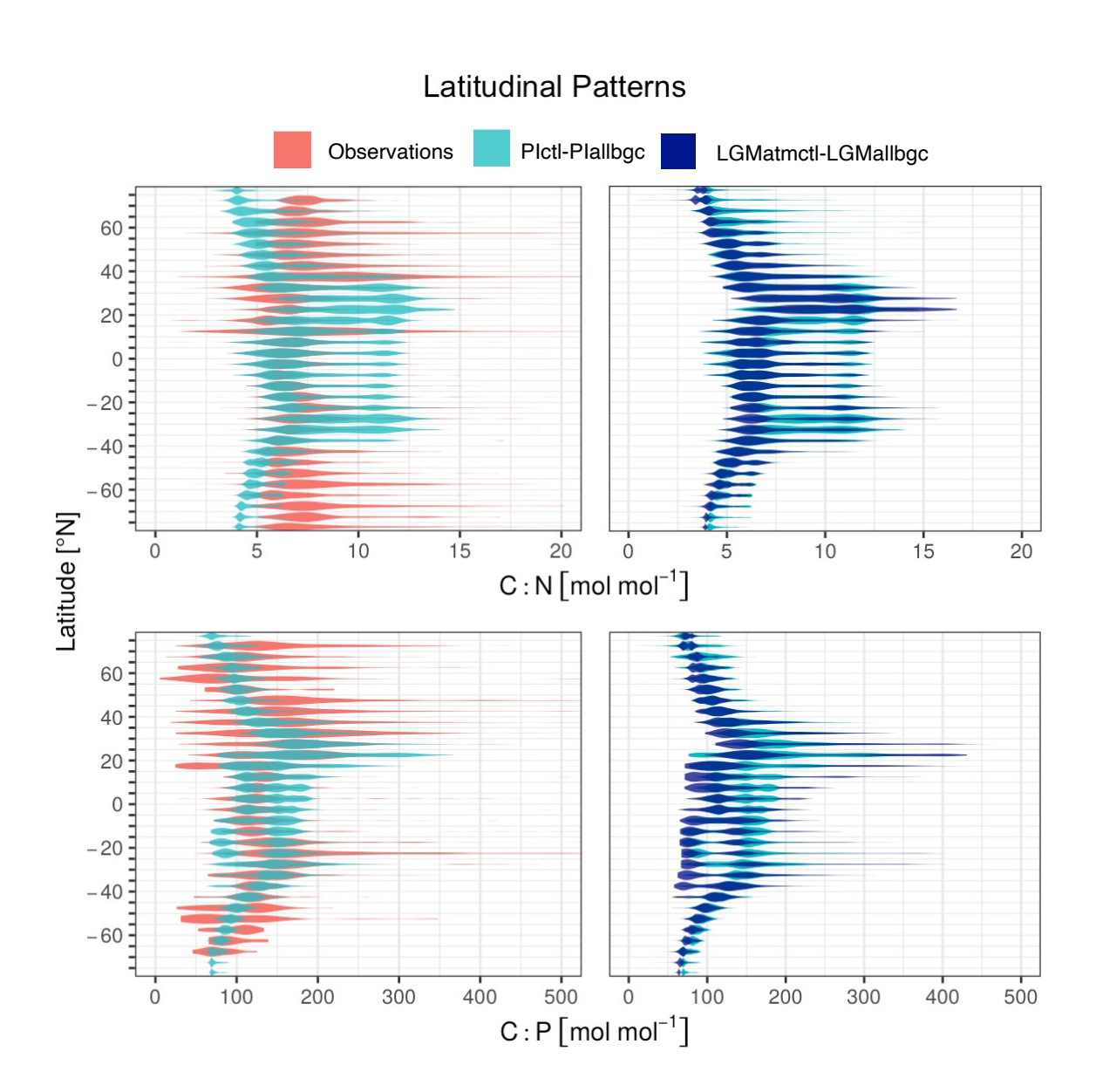


Figure 4. Observed and simulated latitudinal patterns of carbon-to-nitrogen (C:N) and carbon-to-phosphorus (C:P) ratios in particulate organic matter (POM). Observations in the left panels refers to the compilation by Tanioka et al. (2022). Model results represent the mean values from the 20 simulations in Pictl-Piallbgc and LGMatmctl-LGMallbgc.





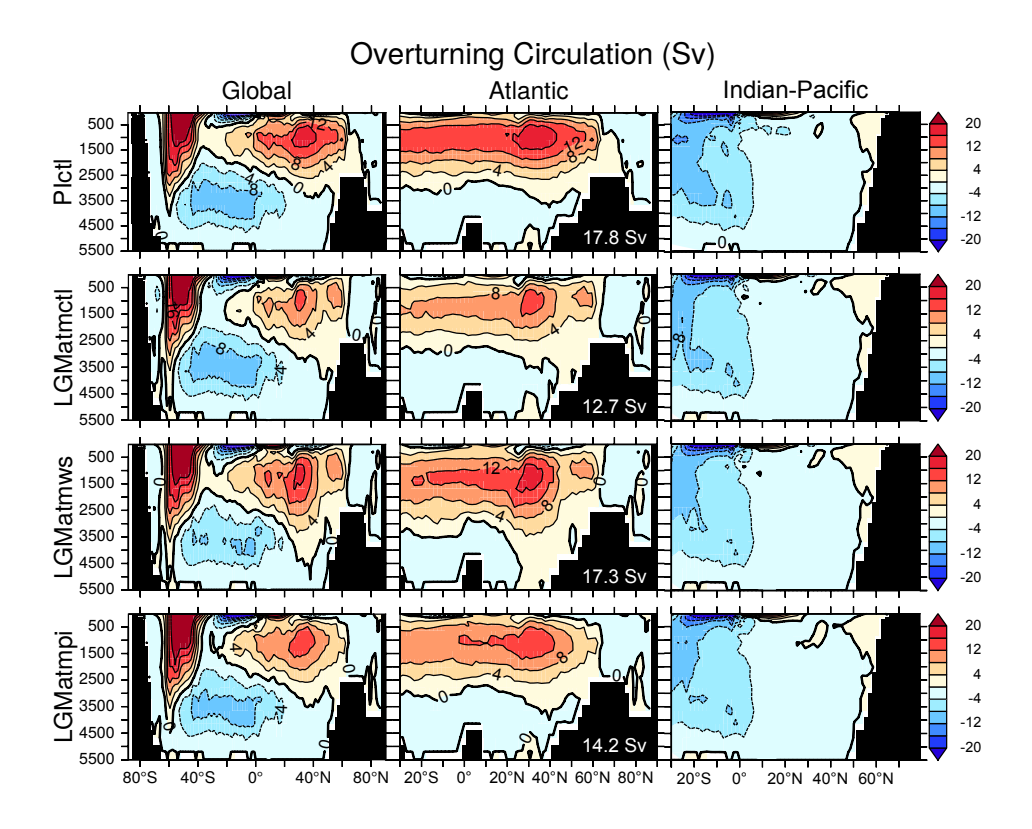


Figure 5. Meridional overturning streamfunction in the Global, Atlantic, and Indian-Pacific Oceans for PIctl, LGMatmctl, LGMatmws, and LGMatmpi, all combined with the PIallbgc biogeochemical configuration. Results are ensemble means over the 20 simulations in each of the configurations. Values in white indicate the strength of maximum AMOC at 26.5°N under each condition.

PIallbgc, LGMatmws-PIallbgc, and LGMatmpi-PIallbgc are 12.66 ± 0.01 Sv at 1400 m, 17.33 ± 0.04 Sv at 1700 m, and 14.16 ± 0.03 Sv at 1100 m, respectively (Fig. 5).

The model results show only small changes in the MOC of the Indian and Pacific Oceans, with close agreement between LGMatmctl-PIallbgc and PIctl-PIallbgc, indicating that the effect of the LGM lower surface temperature and lower atmospheric pCO $_2$ (250.2 \pm 3.2 ppm) is almost compensated by the LGM winds and atmospheric moisture diffusivity. As a consequence of the virtual insensitivity of the Indo-Pacific MOC to a switch from pre-industrial to LGM boundary conditions, changes in the global MOC essentially mirror the changes in the AMOC (Fig. 5).

3.2.2 Dissolved iron

175

For the pre-industrial control (PIctl) with PI biogeochemistry (PIctl-PIallbgc), the ensemble average (employing the 20 lowest-cost parameter sets) of globally-averaged dissolved Fe (dFe) concentration is $596 \pm 14 \,\mathrm{nmol}\,\mathrm{m}^{-3}$. This value is only slightly lower than the observational estimate of $624 \,\mathrm{nmol}\,\mathrm{m}^{-3}$ for the modern ocean from Huang et al. (2022) (Fig. 6a, Table S1). In





the *-LGMFedep configurations, the increased Fe input from enhanced dust deposition results in higher dFe concentrations 180 than all other configurations. The average concentration is $84\,\mathrm{nmol\,m^{-3}}$ (15%) higher than in the *-PIallbgc simulations. In the *-LGMFesed simulations, where sedimentary iron fluxes are reduced due to the lower LGM sea level, average dFe concentration is 198 nmol m⁻³ (35 %) lower than in the *-PIallbgc simulations, and the lower Fe availability has a great impact on productivity and export of particulate organic carbon (POC). The dFe concentrations in the *-LGMPO4 and *-LGMbdeni simulations are all similar to those of the PIctl-PIallbgc baseline, indicating that changes in phosphorus and nitrogen cycling 185 have minimal impact on dFe inventories, with Fe availability remaining relatively stable. In *-LGMallbgc simulations, the increased Fe deposition and reduced sedimentary input result in 6 nmol m⁻³ (1%) decrease in dFe concentration (Fig. 6a, Table S1). Differences in dFe between physical configurations for the same biogeochemistry are much smaller than between biogeochemical configurations (Fig. 6a and 7a). Interestingly, in all LGM physical configurations, dFe is lower than in the 190 corresponding PIctl-* configurations (Fig. 7i). In the model, sedimentary Fe input is associated with the POC flux at the sea floor. Since the POC export declines under LGM conditions due to the lower temperature and lower surface nutrients, sedimentary Fe inputs and consequently the dFe inventories are lower in the LGM than in the PIctl simulations.

Surface dFe (sdFe, 0–50 m) shows similar but more accentuated pattern changes compared to globally-averaged dFe, except that the LGMatmctl-* configurations have higher sdFe than the other LGM physical configurations for the same biogeochemistry (Fig. 6b, Table S1). The overall variation in sdFe is also similar to that of globally-averaged dFe. In *-LGMFedep, the sdFe is $198 \, \mathrm{nmol} \, \mathrm{m}^{-3}$ (54%) higher than in *-PIallbgc, and this difference is greater than the $84 \, \mathrm{nmol} \, \mathrm{m}^{-3}$ (15%) for the globally-averaged dFe (Fig. 7a, b and Table S1). These results highlight the significant role of atmospheric Fe deposition in controlling sdFe concentrations.

3.2.3 Nitrate

205

The average NO_3^- concentration in the *-LGMFesed simulations is $31.4 \,\mathrm{mmol\,m^{-3}}$, significantly lower than the $22.1 \,\mathrm{mmol\,m^{-3}}$ in *-PIallbgc (Figs. 6c and 7c). This reduction is likely due to a lower iron availability in *-LGMFesed, which limits N_2 fixation. Indeed, the global N_2 fixation rates are also significantly lower than for *-PIallbgc (Fig. 6k and 8c and Table S1). Surprisingly, while dFe availability affects N_2 fixation, simulations with higher dFe supply and concentrations do not always result in higher NO_3^- inventories. For example, the average NO_3^- concentration for *-LGMFedep is $2.0 \,\mathrm{mmol\,m^{-3}}$ lower than for *-PIallbgc. This is because of the changes in Fe supply in the model do not only affect N_2 fixation, but can induce changes in denitrification that in turn depend on the level and consumption of oxygen in association with the attenuation of the exported particulate organic matter (POM). Two NO_3^- sinks occur in the model. One is water-column (WC) denitrification, which is affected by WC O_2 supply and consumption via POM remineralisation. The other is benthic denitrification, which is determined by the POC flux at the sea floor. Thus, both water column and benthic denitrification are affected by the POM export. The higher Fe supply in the surface ocean increases not only N_2 fixation but also net primary production (NPP) and particulate organic matter (POM) export, and consequently promotes both water-column and benthic denitrification. The net effect on the NO_3^- inventory depends on the balance of these counteracting fluxes. Whenever NO_3^- concentrations are lower in a simulation in *-LGMFedep, the increase in denitrification is higher than the increase in N_2 fixation at the beginning of





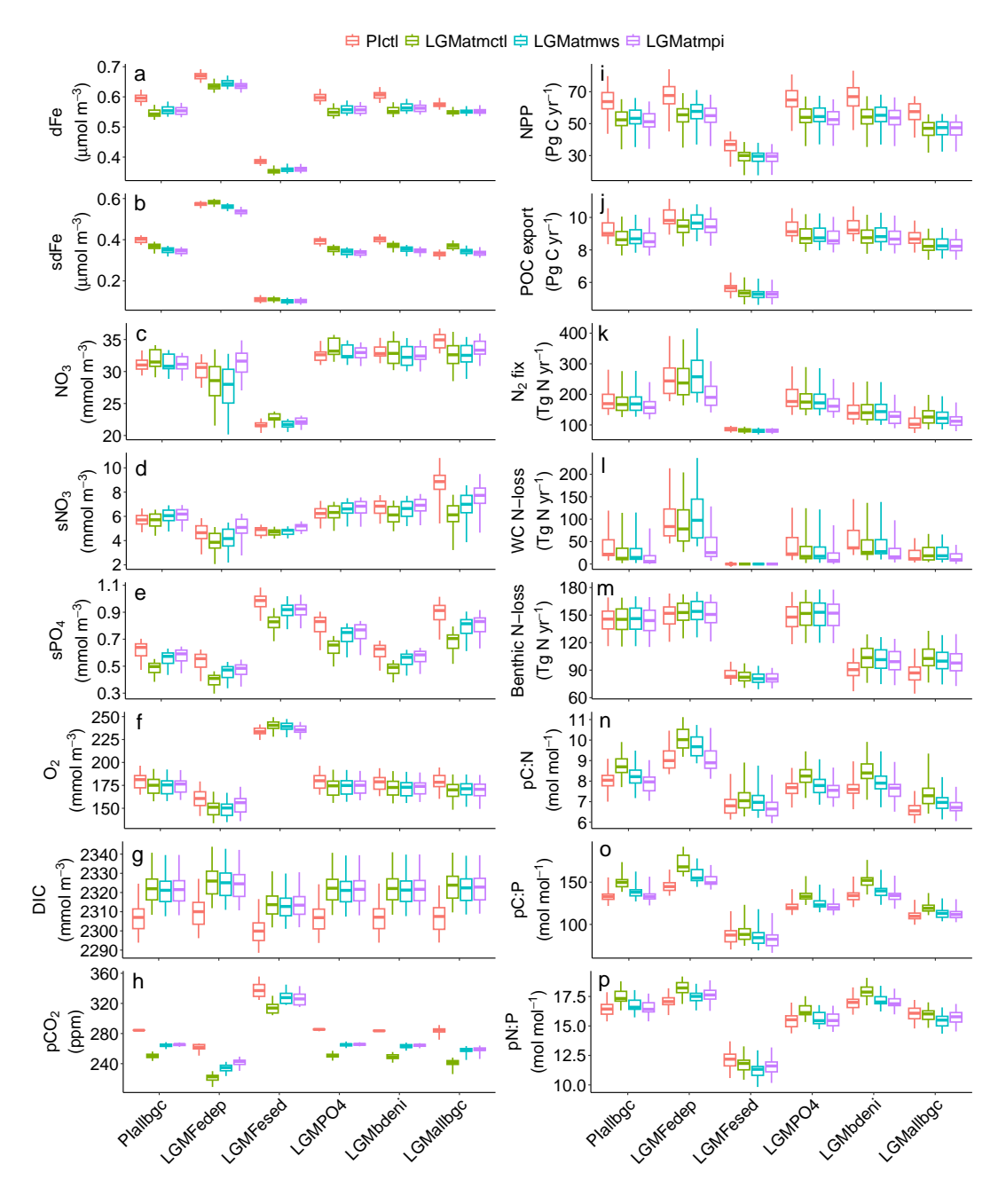


Figure 6. Globally-averaged (a) dissolved iron (dFe), (b) surface dFe (sdFe), (c) NO₃⁻, (d) surface NO₃⁻ (sNO₃⁻), (e) surface PO₄³⁻ (sPO₄³⁻), (f) O₂, (g) DIC, (h) pCO₂, (i) globally-integrated net primary production (NPP), (j) particulate organic carbon (POC) export at 130 m depth, (k) N₂ fixation (N₂ fix), (l) water column denitrification (WC N–loss), (m) benthic denitrification (benthic N–loss), and global medians of surface (n) particulate carbon to nitrogen (pC:N), (o) carbon to phosphorus (pC:P), and (p) nitrogen to phosphorus (pN:P) ratios of the 20 simulations in each of the 24 model configurations. The lower, middle, and upper hinges indicate the first, second, and third quartiles, respectively, representing the spread of solutions of the 20 ensemble members. The whiskers here extend to the minimum and maximum values. Data from ice-covered area were excluded for the particulate elemental ratios, because there extremely low POC could cause unrealistically low pC:N and pC:P values.





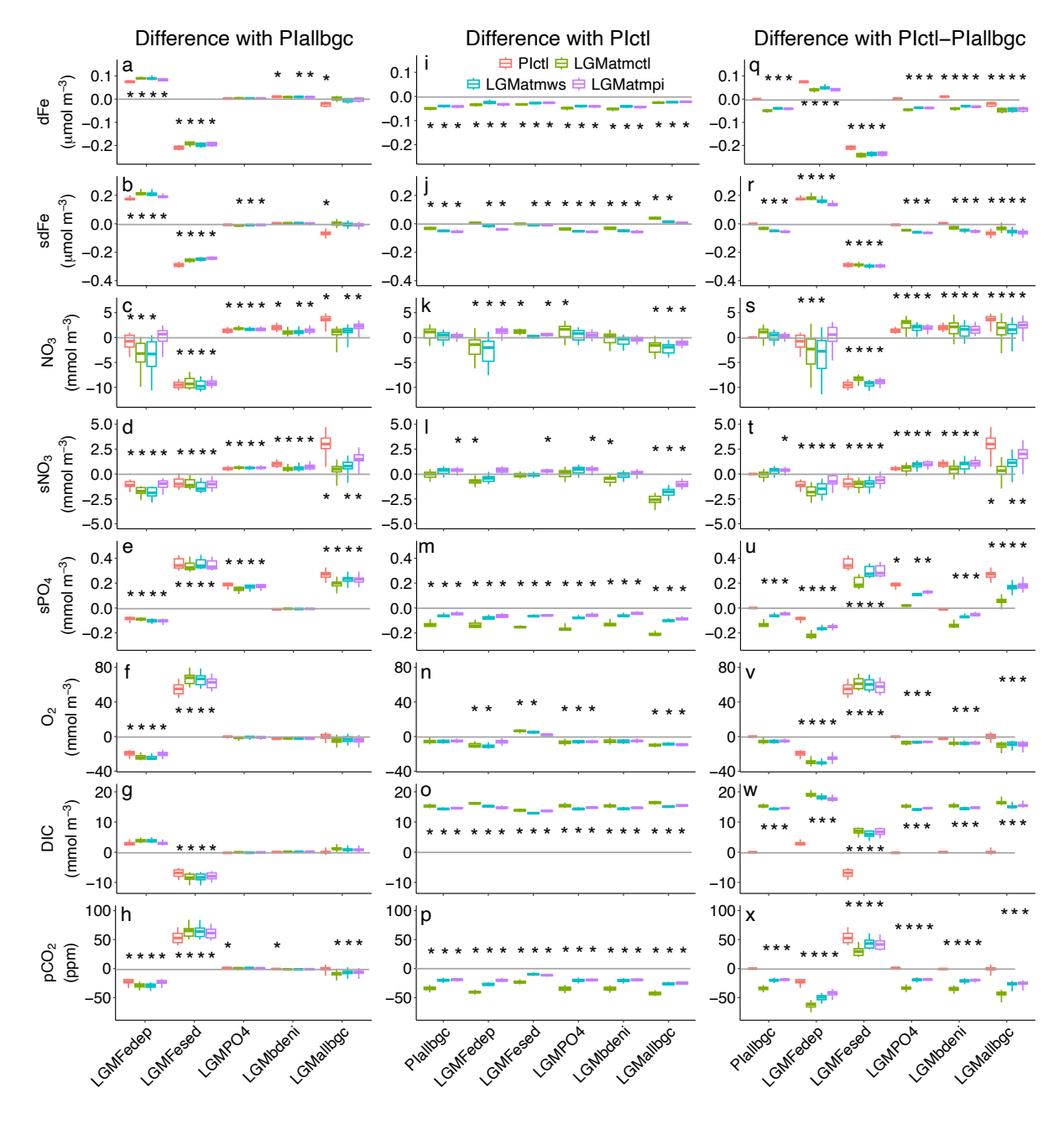


Figure 7. Differences in globally averaged tracer concentrations with respect to default biogeochemical conditions (PIallbgc, left panels), preindustrial physical conditions (PIctl, mid panels), and the pre-industrial reference condition (PIctl-PIallbgc, right panels). The panels show (from top to bottom) globally-averaged dissolved Fe (dFe), surface dFe (sdFe), NO₃⁻, surface NO₃⁻ (sNO₃⁻), surface PO₄³⁻ (sPO₄³⁻), O₂, DIC, and atmospheric pCO₂ for the 20 simulations in each of the physical and biogeochemical configurations. The lower, middle, and upper hinges indicate the first, second, and third quartiles, respectively. The whiskers here extend to the minimum and maximum values. Stars indicate significant differences between the groups being compared (P-value <0.05, Student's t-test). Horizontal gray lines indicate no difference from the tracer values under pre-industrial conditions.



215

220

225

230

235



the spin-up, because the increase in N_2 fixation due to a higher Fe supply is hampered by the supply of the other limiting nutrient, PO_4^{3-} . In that situation, the model simulates a lower NO_3^{-} inventory once the simulation reaches equilibrium despite an increase in N_2 fixation. This explains that while global N_2 fixation in *-LGMFedep simulations is higher than for *-PIallbgc (Fig. 8c, Table S2), the NO_3^{-} inventories in *-LGMFedep show a mixed response (Fig. 7c, Table S1). Interestingly, the NO_3^{-} differences to PIctl-* in the *-LGMFedep simulations are much more variable than for the other biogeochemical configurations (Fig. 7k, Table S1). This shows that increasing dFe supply enhances the sensitivity of N_2 fixation and denitrification fluxes to changes in physical boundary conditions. These results highlight both the critical role of iron availability in regulating the global NO_3^{-} inventory and the importance of the interplay between the biogeochemical and physical boundary conditions in controlling the balance of NO_3^{-} gains and losses in the ocean.

The enhanced N_2 fixation due to the greater phosphate availability in *-LGMPO₄ and the reduced benthic denitrification in *-LGMbdeni both produce higher NO_3^- inventories than *-PIallbgc (Fig. 7c, Table S1). The NO_3^- inventories in *-LGMallbgc on average is 2.0 mmol m^{-3} higher than in *-PIallbgc across all physical configurations (Fig. 7c, Table S1). Although NO_3^- inventories in *-LGMFesed are reduced, mainly due to a lower sedimentary flux of dFe, dFe supply from atmospheric deposition in *-LGMallbgc seems to compensate that effect. In LGMatmctl-LGMallbgc simulations, the average NO_3^- concentration is 32.9 mmol m^{-3} , which is 1.8 mmol m^{-3} (6%) higher than for PIctl-PIallbgc (Fig. 7s and Table S1), and an increase in deepwater NO_3^- concentrations is also observed (Fig. 3). The increase in NO_3^- from PIctl-PIallbgc to LGMatmctl-LGMallbgc is lower than the estimates based on paleo proxies (>10%, Glock et al., 2018; Wallmann et al., 2016; Deutsch et al., 2004). Nevertheless, the increase in 5 out of the 20 individual simulations is larger than 10%, and the maximum increase reaches 16% (4.9 mmol m⁻³).

In addition to the counteracting effects of *-LGMallbgc on N_2 fixation and denitrification processes, surface NO_3^- (s NO_3^-) concentrations are also affected by the strength of the ocean circulation and biological utilisation. Therefore, changes in s NO_3^- do not necessarily follow the same pattern as changes in the NO_3^- inventory. Across all physical configurations, while the NO_3^- inventory in the *-LGMFedep simulations is only about 7 % lower than in *-PIallbgc, the difference in s NO_3^- is 24 % (Fig. 7c and d). On the other hand, the NO_3^- inventory in *-LGMFesed is about 30 % lower on average than in *-PIallbgc, but s NO_3^- is only 18 % lower. This apparent inconsistency between changes in NO_3^- inventory and the surface concentration reflects different responses to changes in iron supply.

240 3.2.4 Surface phosphate

The mean surface PO_4^{3-} (sPO₄³⁻) in PIctl-PIallbgc is 0.62 ± 0.07 mmol m⁻³, which is close to the 0.56 mmol m⁻³ in WOA2013 (Garcia et al., 2013b) (Fig. 6e and Table S1). In the *-LGMPO₄ simulations, sPO₄³⁻ on average is 0.73 mmol m⁻³, about 31 % higher than in *-PIallbgc, which is more than the 15 % increase in the inventory, indicating a non-linear relationship between sPO₄³⁻ and its global inventory (Fig. 3, 7e and Table S1). The average sPO₄³⁻ in the *-LGMFedep simulations is 0.46 mmol m⁻³, about 17 % lower than in the *-PIallbgc simulations, which can be attributed to a higher biological PO_4^{3-} utilisation for elevated dFe supply. The average sPO₄³⁻ in the *-LGMFesed simulations is 0.90 mmol m⁻³, about 62 % higher than in *-PIallbgc, even higher than in *-LGMPO₄. The *-LGMbdeni simulations produce sPO₄³⁻ of 0.55 mmol m⁻³, and



250

260

265



in *-LGMallbgc it is 0.78 mmol m^{-3} . These results indicate that Fe supply is a critical factor that affects sPO_4^{3-} , whereas changes in NO_3^{-} cycling alone have relatively minor effects. Changes in ocean circulation also affect sPO_4^{3-} . For example, for all the biogeochemical configurations, sPO_4^{3-} for LGMatmws, LGMatmpi and particularly LGMatmctl are lower than for PIctl (Fig. 7m).

3.2.5 Dissolved oxygen

The average dissolved marine oxygen (O_2) concentration in the PIctl-PIallbgc simulations is $179 \pm 9 \text{ mmol m}^{-3}$. The O_2 inventories in the LGM simulations show considerable variability, with some simulations exhibiting significant deviations from *-PIallbgc (Fig. 7f). The *-LGMFesed configurations, which feature reduced iron input, result in a remarkable increase of 62 mmol m^{-3} in O_2 concentrations (Fig. 7f), consistent with reduced water column denitrification and benthic denitrification because of the much reduced NPP and POC export. Conversely, O_2 in the *-LGMFedep simulations is 22 mmol m^{-3} lower. The *-LGMPO₄ and *-LGMbdeni simulations produce oxygen concentrations close to *-PIallbgc, and across physical conditions the differences with respect to *-PIallbgc on average are $1.0 \text{ and } 2.3 \text{ mmol m}^{-3}$ lower, respectively. These results suggest that changes in PO_4^{3-} and NO_3^{-} availability alone have limited effects on the O_2 inventory. Overall, the average O_2 in *-LGMallbgc simulations is $172 \pm 5 \text{ mmol m}^{-3}$, about 2 % lower than in *-PIallbgc simulations.

Among the LGM physical configurations, O_2 levels generally are lower than in the respective PIctl-* simulations. For example, the average concentration for LGMatmctl-* is $180 \, \mathrm{mmol \, m^{-3}}$, $5.2 \, \mathrm{mmol \, m^{-3}}$ (2.8%) lower than for PIctl-*. When compared LGMatmctl-LGMallbgc to PIctl-PIallbgc, the global O_2 decreases by $10 \, \mathrm{mmol \, m^{-3}}$, which is due to the depletion in the deep water, while the upper ocean concentrations are typically higher (Fig. 3). This agrees with estimated LGM O_2 levels based on paleo proxies (Jaccard and Galbraith, 2012; Anderson et al., 2019) and model simulations (Bopp et al., 2017; Somes et al., 2017). An exception is the *-LGMFesed simulations , where O_2 levels are higher than in the PIctl-* simulations, which indicates a strong coupling with dFe reduction and changes in physical boundary conditions (Fig. 7n).

3.2.6 Dissolved inorganic carbon and atmospheric pCO₂

In the *-LGMFesed simulations, globally-averaged DIC is 7.8 mmol m⁻³ lower than in the corresponding *-PIallbgc simulations (Fig. 7g). This decrease in DIC is likely linked to reduced primary production and carbon export, as Fe availability is a critical limiting factor for these processes. In contrast, the *-LGMFedep simulations have higher DIC. This can be attributed to increased primary production and carbon export driven by the iron fertilisation effect, leading to greater uptake of CO₂ from the atmosphere and increased carbon storage in the ocean. The *-LGMPO₄ and *-LGMbdeni simulations yield DIC concentrations similar to those of the pre-industrial control. These findings indicate that iron inputs, whether from atmospheric deposition or sedimentary sources, play a critical role in regulating the global DIC inventory. Our LGM simulations yield higher DIC concentrations than the PIctl-* simulations throughout the different biogeochemical configurations (Fig. 7o). Also, the increase in DIC is mostly observed in the deep water (Fig. 3). Further, DIC concentrations within each of the LGM physical configurations are similar, despite the different strength of overturning circulation (Fig. 5 and 7g). The glacial-interglacial changes in the strength of the solubility pump caused by a reduced temperature, for example, can be obtained by comparing simulated results



290

295

300

305



from PIctl-PIallbgc and LGMatmpi-PIallbgc. The latter shows an average increase of $14.6 \,\mathrm{mmol}\,\mathrm{m}^{-3}$ (0.6%) in DIC, which is equivalent to 238 Pg of carbon.

Atmospheric pCO₂ in the biogeochemically coupled but radiatively uncoupled 20 PIctl-PIallbgc simulations is 284.4 ± 0.1 ppm, consistent with the radiatively prescribed 284.3 ppm that was used for the calibration stage (Fig. 6h and Table S1). This indicates equilibrated carbon fluxes between air, land and ocean carbon pools at the end of the spin-ups. Switching to LGM Fe fluxes has a relatively strong effect on pCO₂, when compared to the effects of the LGM PO₄³⁻ inventory or benthic denitrification. For each of the 4 physical configurations (PIctl, LGMatmetl, LGMatmws, and LGMatmpi, Table 2a), the difference of employing the biogeochemical LGM forcing conditions with respect to the biogeochemical *-PIallbgc in pCO₂ are most pronounced for *-LGMFesed, where pCO₂ increases by 60 ppm, and *-LGMFedep, showing a decrease by 26 ppm (Fig. 7h and Table S1).

The average atmospheric pCO₂ in the physical LGM configurations, LGMatmctl, LGMatmws, and LGMatmpi, are all lower than the respective simulations for PIctl across all biogeochemical configurations. The average differences to PIctl in the LGMatmctl, LGMatmws, and LGMatmpi simulations are -35, -21, and -19 ppm, respectively (Fig. 6h and 7p). The pCO₂ in the 20 LGMatmctl-LGMallbgc simulations ranges from 226 to 248 ppm, with an average of 241 ppm.

Atmospheric pCO₂ shows different levels of variability among the 20 simulations within each of the biogeochemical configurations. The difference between the maximum and minimum pCO₂ is largest for *-LGMFesed, ranging from 26 ppm in LGMatmctl-LGMFesed to 31 ppm in PIctl-LGMFesed (Fig. 7h). The atmospheric pCO₂ is also influenced by changes in the terrestrial carbon pool. While all LGM physical configurations lead to reduced terrestrial carbon due to changes in radiative forcing, the three LGM atmospheric configurations result in different surface temperature distributions, which in turn affect the amount of carbon released to the atmosphere and ocean. The carbon released from land in the LGMatmctl, LGMatmws, and LGMatmpi simulations are 177 ± 1 , 190 ± 0 , and 198 ± 1 Pg C, respectively. When considering the combined carbon loss from land and the atmosphere, the ocean carbon storage in the LGMatmctl, LGMatmws, and LGMatmpi simulations are 251 ± 15 , 234 ± 13 , and 239 ± 9 Pg C higher than in the PIctl simulations, respectively. Of the changes in ocean carbon inventories, changes in atmospheric carbon account for approximately 30 %, 18 %, and 17 % in the LGMatmctl, LGMatmws, and LGMatmpi simulations, respectively.

3.3 Biogeochemical rate estimates and elemental composition of POM

3.3.1 Marine NPP and POC export

Net primary production (NPP) in PIctl-PIallbgc ranges from 44 to $80 \, \mathrm{Pg} \, \mathrm{Cyr}^{-1}$, with mean and standard deviation of $64 \pm 8 \, \mathrm{Pg} \, \mathrm{Cyr}^{-1}$ (Fig. 6i and Table S2), in line with observational estimates ($36 - 77 \, \mathrm{Pg} \, \mathrm{Cyr}^{-1}$, Carr et al., 2006; Honjo et al., 2008; Buitenhuis et al., 2013). Increasing Fe deposition enhances NPP by about $2.8 \, \mathrm{Pg} \, \mathrm{Cyr}^{-1}$ in the *-LGMFedep simulations when compared with *-PIallbgc, slightly more than the increases of $1.5 \, \mathrm{Pg} \, \mathrm{Cyr}^{-1}$ in *-LGMPO₄ and $1.8 \, \mathrm{Pg} \, \mathrm{Cyr}^{-1}$ in *-LGMbdeni (Fig. 8a). A strong reduction in NPP is associated with the reduced sedimentary Fe flux in the *-LGMFesed simulations, where NPP is about $24 \, \mathrm{Pg} \, \mathrm{Cyr}^{-1}$ (44 %) lower on average than in *-PIallbgc (Fig. 8a). Nevertheless, NPP in *-LGMallbgc is only



320

325

330



6.0 Pg Cyr⁻¹ (11%) lower than in *-PIallbgc. Due to the lower temperatures, NPP decreases by 10.7 Pg Cyr⁻¹ (18%) on average among all the LGM physical configurations compared to PIctl (Fig. 8i). Switching to LGM moisture diffusivity and wind pattern has no noticeable effect on NPP.

Particulate organic carbon (POC) export shows a similar pattern to that of NPP. The average flux in the PIctl-PIallbgc simulations is $9.2\pm0.6\,\mathrm{Pg\,Cyr^{-1}}$ (Fig. 6j, Table S2). POC export increases by $0.8\,\mathrm{Pg\,Cyr^{-1}}$ (9%) for *-LGMFedep and decreases by $3.5\,\mathrm{Pg\,Cyr^{-1}}$ (39%) for *-LGMFesed, with only small changes in *-LGMPO₄, *-LGMbdeni, and *-LGMallbgc when compared with *-PIallbgc (Fig. 8b). The reduction in POC export due to a cooler climate is $0.5\,\mathrm{Pg\,Cyr^{-1}}$ (5%) among the LGM physical configurations.

3.3.2 Marine N_2 fixation and water-column and benthic denitrification

 N_2 fixation rates in PIctl-PIallbgc range from 132 to 281 $Tg\,N\,yr^{-1}$ (Fig. 6k), agreeing with observations (223 \pm 30 $Tg\,N\,yr^{-1}$, Shao et al., 2023), and inverse-model estimates (126 – 223 $Tg\,N\,yr^{-1}$, Wang et al., 2019). WC denitrification rates vary strongly among the PIctl-PIallbgc simulations, ranging from 8 to $119\,Tg\,N\,yr^{-1}$, and benthic denitrification rates range from 116 to $169\,Tg\,N\,yr^{-1}$ (Fig. 6l and m), also in line with previous estimates (39 to 66 and 68 to 122 $Tg\,N\,yr^{-1}$ for WC and benthic denitrification rates, respectively, Eugster et al., 2013).

In the model, N_2 fixation is the counterpart of WC and benthic denitrification, thus N_2 fixation equals the sum of WC and benthic denitrification at equilibrium. Across our physical configurations, N_2 fixation increases by 65 $TgNyr^{-1}$ (37%) on average in *-LGMFedep simulations compared with *-PIallbgc, due to the extra input of Fe relieving iron limitation of diazotrophs (Fig. 8c). WC denitrification is 56 $TgNyr^{-1}$ (197%) higher (Fig. 8d), compensating for most of the increase in N_2 fixation, and benthic denitrification only increases by 8 $TgNyr^{-1}$ (5%, Fig. 8e). N_2 fixation drops by 93 $TgNyr^{-1}$ (53%) on average in the *-LGMFesed simulations, while benthic denitrification decreases by 62 $TgNyr^{-1}$ (43%) and WC denitrification shuts down entirely.

In the *-LGMPO₄ simulations, N_2 fixation and the sum of denitrification increase by 8 TgNyr⁻¹ (5%) compared to *-PIallbgc (Fig. 8c). Benthic denitrification decreases by 46 TgNyr⁻¹ (31%) on average in the *-LGMbdeni simulations, while WC denitrification increases by 15 TgNyr⁻¹ (52%), and N_2 fixation is 31 TgNyr⁻¹ (18%) lower than in *-PIallbgc. In *-LGMallbgc, N_2 fixation and WC and benthic N denitrification decrease by 55 (31%), 6 (22%), and 47 TgNyr⁻¹ (33%), respectively (Fig. 8c, d and e).

340 3.3.3 Elemental composition of POM

The elemental ratios of particulate organic matter (POM) provide insights into nutrient utilisation efficiency and the coupling between carbon, nitrogen, and phosphorus in marine ecosystems. Here we analyse the particulate carbon to nitrogen (pC:N), carbon to phosphorus (pC:P), and nitrogen to phosphorus (pN:P) ratios. The ecological elemental ratios do not follow normal distributions, and we calculate median of the elemental ratios without biomass wighting in the ocean gird cells that are not covered by ice, rather than mean values to avoid unnecessary bias (Isles, 2020). The global median of surface (0 - 50 m) pC:N, pC:P, and pN:P in the PIctl-PIallbgc simulations are $8.0 \pm 0.5 \text{ mol mol}^{-1}$, $134 \pm 8 \text{ mol mol}^{-1}$, and $16.5 \pm 0.7 \text{ mol mol}^{-1}$,





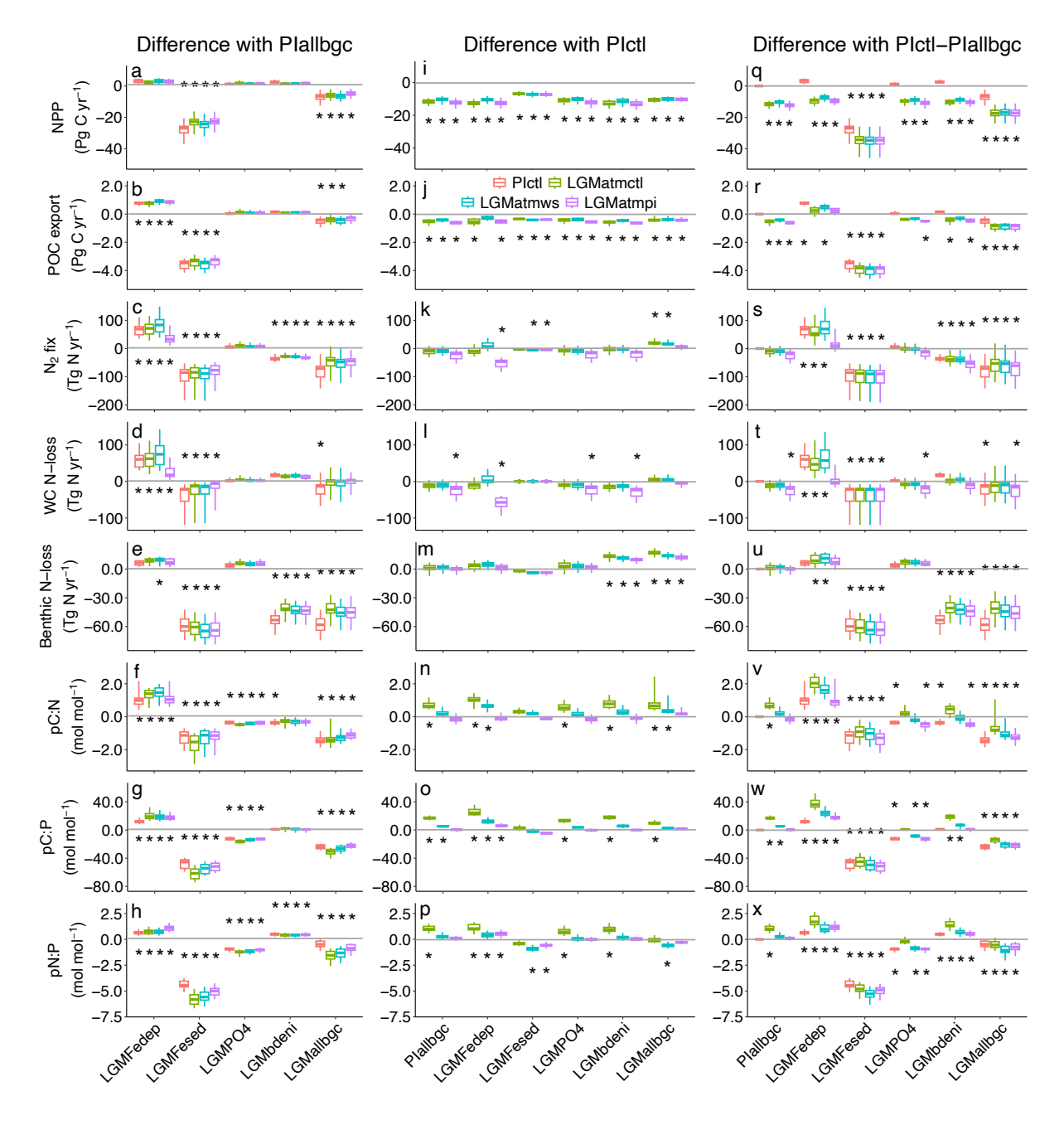


Figure 8. Differences in fluxes and elemental ratios with respect to default biogeochemical conditions (PIallbgc, left panels), pre-industrial physical conditions (PIctl, mid panels), and the pre-industrial reference condition (PIctl-PIallbgc, right panels). The panels show (from top to bottom) net primary production (NPP), particulate organic carbon (POC) export, N_2 fixation (N_2 fix), water-column denitrification (WC N-loss), benthic N-loss, and particulate organic nitrogen to carbon (pN:C), phosphorus to carbon (pP:C), and nitrogen to phosphorus (pN:P) ratios for the 20 simulations in each of the physical and biogeochemical configurations. The lower, middle, and upper hinges indicate the first, second, and third quartiles, respectively. The whiskers here extend to the minimum and maximum values. Stars indicate significant differences between the groups being compared (P-value <0.05, Student's t-test). The gray lines indicate zero change for each flux or ratio.



350

355

360

365

370



respectively (Fig. 6n–p, Table S2). When compare different biogeochemical conditions to *-PIallbgc, overall the change in globally-averaged pC:N is negatively correlated with the change in sNO₃⁻ (Figs. 7d and 8f). Nevertheless, the pC:N is lower despite lower sNO₃⁻ in *-LGMFesed (Tables S1 and S2) because of the shrinking area with low sNO₃⁻, caused by low NO₃⁻ utilisation under strong iron limitation, such as the South Pacific Ocean, and hence the area with high pC:N also becomes smaller (Fig. S1). In general, pC:N in the model is mainly affected by two factors. One is the Fe limitation of carbon fixation and NO₃⁻ utilisation, and the other is the supply of NO₃⁻ to the surface ocean.

The relation between pC:P and surface PO_4^{3-} (sPO₄³⁻) is similar to the relation between pC:N and sNO₃⁻ (Fig. 6o). Since the PO_4^{3-} inventory is constant in the model, sPO₄³⁻ is largely affected by the supply of dFe. In LGMatmctl-LGMallbgc simulations, sPO₄³⁻ and sNO₃⁻ are higher than in the PIctl-PIallbgc (Fig. 7t and u), and the pC:N and pC:P are generally lower, particularly in low latitude regions where the surface nutrients are higher (Fig. 4). In *-LGMFesed simulations sPO₄³⁻ increases with lower iron supply. As a result, pC:P in *-LGMFesed simulations decreases by 54 mol mol⁻¹ (39 %), while pC:N decreases by only 1.3 mol mol⁻¹ (16 %) when compared with *-PIallbgc (Fig. 8g and f).

When compared with the average sPO₄³⁻ in *-PIallbgc, the concentration in *-LGMPO₄ simulations is 31 % higher, which is smaller than the 62 % increase in *-LGMFesed. Moreover, the effects of Fe limitation on carbon fixation and nitrogen assimilation in *-LGMPO₄ are not as strong as in *-LGMFesed. As a result, the pC:P and pN:P in *-LGMPO₄ decrease by only 10 % and 6 %, respectively, compared to *-PIallbgc, much less than the decrease seen in *-LGMFesed.

Due to the stronger increase in pC:P relative to pC:N, pN:P decreases by 31 % in *-LGMFesed (Fig. 8h), while other biogeochemical LGM configurations have smaller effects. Physical boundary conditions also contribute to the changes in the elemental ratios of POM via effects on sNO₃⁻ and sPO₄³⁻. The pC:N and pC:P in general are highest for LGMatmctl and lowest for PIctl and LGMatmws, and pN:P is highest in the LGMatmctl configuration (Fig. 8n-p).

4 Discussion

4.1 Effects of biogeochemical boundary conditions on biogeochemistry

Among the four glacial-interglacial changes in biogeochemical boundary conditions investigated, iron supply has the strongest impact on the inventories and fluxes. Clearly, it is the increase in Fe availability within the surface layers (*-LGMFedep) that alleviates iron limitation and stimulates NPP and POC export via the biological pump. Eventually, such changes in the Fe supply also affect O₂, N₂ fixation, denitrification, the NO₃⁻ inventory, and POM elemental ratios. Sedimentary Fe flux in *-LGMFesed is 10.3 Gmol Fe yr⁻¹ (83 %) lower than in PIctl (Fig. 1), which agrees with other modelling estimates (e.g., Muglia et al., 2017). Glacial-interglacial changes in sedimentary Fe input were not considered in several earlier studies (Somes et al., 2017; Ödalen et al., 2020; Matsumoto et al., 2020a, b; Vollmer et al., 2022). Nevertheless, the strong sensitivity of the biogeochemical inventories and fluxes to changes in sedimentary influx of Fe demonstrates its importance. The reduction in sedimentary input of Fe from *-PIallbgc to *-LGMFesed (10.3 Gmol Fe yr⁻¹) is greater than the increase in atmospheric Fe deposition from *-PIallbgc to *-LGMFedep (4.7 Gmol Fe yr⁻¹), resulting in smaller dFe inventories in *-LGMallbgc. One might argue that the sedimentary input is overestimated in the model and thus its decline in the LGM simulations may also



400

405



be too strong. However, the predicted 12.6 GmolFeyr⁻¹ in PIctl-PIallbgc falls close to the lower end of the range of other models (0.6 –194 GmolFeyr⁻¹, Tagliabue et al., 2016). A recent sensitivity study also shows that a much higher present-day sedimentary Fe release (117 GmolFeyr⁻¹) than assumed previously (15 GmolFeyr⁻¹ yields better model-data misfit in global and surface dFe distribution (Somes et al., 2021). The Fesed reduction scenario imposed in this study is thus not necessarily yielding too much drawdown in Fe supply. The lower dFe inventory during the LGM seems in conflict with the general understanding of Fe fertilisation during the LGM (Martin, 1990; Martínez-García et al., 2014). Interestingly, although NPP and POC export are lower in the *-LGMallbgc simulations compared the *-PIallbgc simulations (Table. S1), the corresponding atmospheric pCO₂ in general are lower as well. This indicates that, during the spin-up phase of the *-LGMallbgc simulations, enhanced Fe deposition to the surface ocean was able to increase major nutrient utilisation and stimulated NPP and POC export. However, at equilibrium, both NPP and POC export become lower than those in the *-PIallbgc simulations due to the decreased global temperature.

While earlier works have hypothesised that increased sPO₄³⁻ and sNO₃⁻ during the LGM could have benefited NPP and decreased pCO₂ (Broecker, 1982; Wallmann, 2010; Wallmann et al., 2016), the changes of sPO₄³⁻ in *-LGMPO₄ and sNO₃⁻ in *-LGMbdeni have limited effects on the NPP and pCO₂ in our simulations. The relatively weak effects of the increases in the two major nutrients can be ascribed to (1) co-limitation effects and (2) the variable stoichiometry in UVic-OPEM. PO₄³⁻, NO₃⁻, and Fe are the three limiting nutrients for phytoplankton growth in the model, and nutrient co-limitation is observed in many regions of the ocean (Browning et al., 2017; Browning and Moore, 2023). An increase in PO₄³⁻ or NO₃⁻ alone would trigger or aggravate limitation by the other two nutrients. The flexibility in the carbon to nitrogen (C:N) and carbon to phosphorous (C:P) ratios of phytoplankton in UVic-OPEM further complicates the relationship between NPP and nutrient limitation. When sPO₄³⁻ or sNO₃⁻ increase, pC:P and pC:N decrease in response (Fig. 6 and Table S2), and this partly offsets the effect of increasing major nutrients on NPP and pCO₂.

On the other hand, a stronger Fe supply from atmospheric deposition, as in the LGMFedep condition, could have enhanced the utilisation of PO_4^{3-} and NO_3^{-} , leading to an expansion of the ocean regions depleted in those major nutrients. In such regions, the variable stoichiometry implemented in the model could help sustain NPP by increasing pC:P and pC:N (Fig. 6 and Table S2). This negative feedback mechanism does not exist in models that assume fixed stoichiometry.

These results emphasise the importance of iron as a limiting nutrient, especially during the LGM, when changes in dust deposition and sea level had significant impacts on Fe availability. We also demonstrate that the lower temperatures during the LGM should have reduced NPP and POC export and thus the sedimentary flux of Fe, which also affects the oceanic dFe inventory.

4.2 Interactions between physical and biogeochemical boundary conditions

10 Lower temperatures, different wind patterns, and reduced moisture diffusivity over the Southern Ocean in the three LGM physical configurations result in different general circulation patterns, which affect biogeochemical cycles. The LGM boundary conditions affect inventories and fluxes differently. For example, DIC are 14.7 mmol m⁻³ higher for LGMatmpi-* than for PIctl-*, while the differences between LGMatmws-* and LGMatmpi-*, and between LGMatmctl-* and LGMatmpi-* are only



430



-0.3 mmol m⁻³ and 0.8 mmol m⁻³, respectively (Fig. 7o). On the other hand, when compared with PIctl-*, changes in N₂ fixation for LGMatmpi-*, LGMatmws-*, and LGMatmctl-* are -19, 20, and 18 Tg N yr⁻¹, respectively. These indicate that, in our experiments, the glacial-interglacial changes in DIC inventory are dominated by the lower temperature, while the N₂ fixation is affected differently by the three physical conditions.

Across all biogeochemical conditions, our LGM configurations have lower pCO₂ by -35, -21, and -19 ppm in LGMatmctl-*, LGMatmws-*, and LGMatmpi-*, respectively. Thus, the LGM wind pattern and moisture diffusivity over the Southern Ocean contribute about 16 ppm, similar to the 19 ppm drawdown of pCO₂ owing to the lower temperature.

We also notice that the effects of the biogeochemical configurations depend on which physical configuration they are combined with and vice versa. For example, pCO₂ decreases by 0.8 ppm from PIctl-PIallbgc to PIctl-LGMallbgc, by 9.3 ppm from LGMatmctl-PIallbgc to LGMatmctl-LGMallbgc, by 34.2 ppm from PIctl-PIallbgc to LGMatmctl-LGMallbgc.

425 4.3 NO₃⁻ and O₂ levels as constraints for simulating LGM conditions

During the LGM, O_2 and NO_3^- levels and distributions in the ocean were different from the pre-industrial era. According to paleo proxy data, O_2 was lower during the LGM (Jaccard and Galbraith, 2012; Jacobel et al., 2020; Anderson et al., 2019), and NO_3^- was higher (Deutsch et al., 2004; Wallmann et al., 2016; Glock et al., 2018). Globally-averaged O_2 and NO_3^- in LGMatmctl-LGMallbgc simulations are $10 \, \text{mmol} \, \text{m}^{-3}$ lower and $1.8 \, \text{mmol} \, \text{m}^{-3}$ higher on average than in PIctl-PIallbgc (Table S1). In some of the *-LGMFedep simulations, O_2 and NO_3^- levels both become lower than in PIctl-PIallbgc (Fig. 9). In these simulations, high iron input from the atmosphere increases POM production and export, and the ensuing consumption of O_2 causes more widespread oxygen deficient zones, where denitrification occurs.

Such a decrease in NO₃⁻ as simulated by some of the experiments is in conflict with the observational records. Thus, a low NO₃⁻ inventory indicates that a strong decrease in pCO₂ might be due to the wrong reasons in the model, e.g., overestimation of the marine biological carbon pump. On the other hand, the strong Fe limitation in *-LGMFesed simulations results in a decrease in NO₃⁻ due to suppressed N₂ fixation, an increase in pCO₂ due to reduced primary production, and higher O₂ concentrations as a result of lower O₂ consumption from POM export (Fig. 9). Those different NO₃⁻, O₂, and pCO₂ values highlight the critical role of Fe supply for the LGM model experiments.

4.4 Changes in atmospheric pCO₂ and elemental ratio shifts in POM

In the LGMatmctl-LGMallbgc configuration, the average pCO₂ is 43.5 ppm lower than in PIctl-PIallbgc (Fig. 7x and Table S1). The biogeochemical boundary conditions combined contribute less than the physical boundary conditions. The changes in pCO₂ from *-PIallbgc to *-LGMallbgc (biogeochemical) with PIctl and LGMatmctl configurations are -0.8 and -9.3 ppm, respectively, while the changes from PIctl to LGMatmctl (physical) with *-PIallbgc and *-LGMallbgc conditions are -34.2 and -42.7 ppm, respectively (Table S1). The decreasing pCO₂ due to the LGM physical configuration with *-PIallbgc (-34.2 ppm, PIctl-PIallbgc to LGMatmctl-PIallbgc) agrees with a 33 ppm decrease in a previous model experiment considering changes in physical boundary conditions (Ödalen et al., 2020). Nevertheless, the contribution from the LGM biogeochemical boundary



455

460



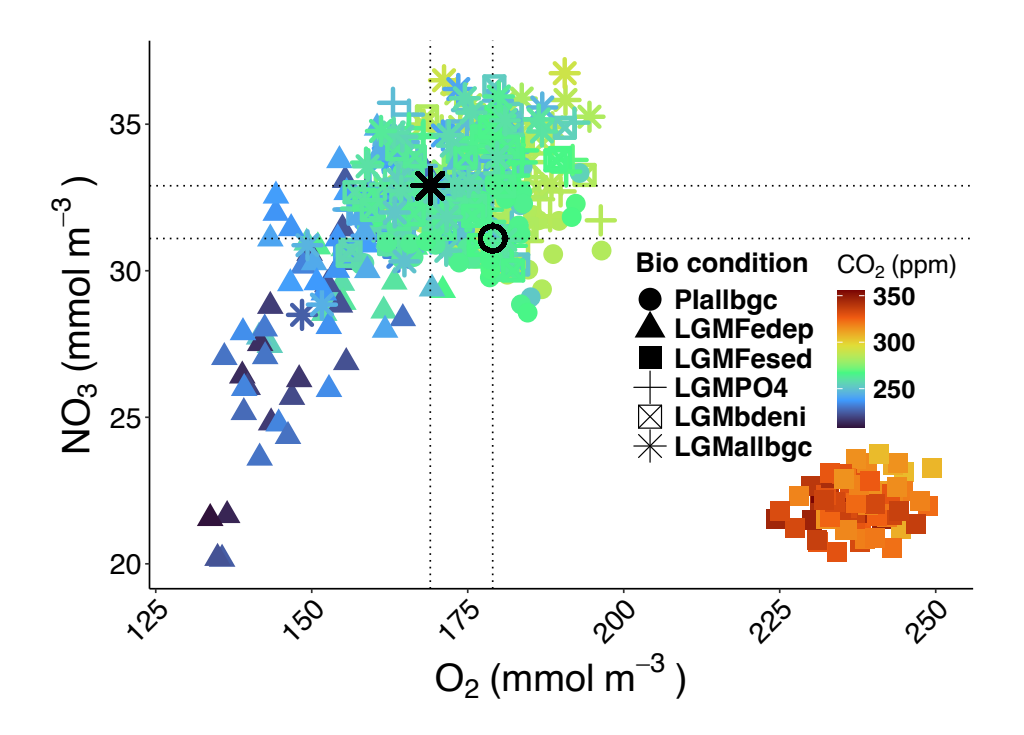


Figure 9. Globally-averaged NO_3^- vs. O_2 in the 480 simulations. Color represents atmospheric pCO₂ and symbols indicate the different biogeochemical configurations. The black open circle and asterisk indicate mean NO_3^- and O_2 in PIctl-PIallbgc and LGMatmctl-LGMallbgc simulations, respectively. The cluster of points with high pCO₂ and low NO_3^- is from *-LGMFesed simulations.

conditions (*-PIallbgc to *-LGMallbgc) to the decrease in pCO₂ is small, and the 43.5 ppm decrease from PIctl-PIallbgc to LGMatmctl-LGMallbgc are only about 50 % of the observed (\approx 90 ppm). The main goal of our experiments is to evaluate changes in some biogeochemical and physical aspects that could affect pCO₂, and not all processes, such as brine-induced stratification (Bouttes et al., 2011) and air-sea disequilibrium (Khatiwala et al., 2019), are considered. These missing processes might also contribute to the ocean receiving less carbon from terrestrial sources than suggested by observational estimates. In our simulations, terrestrial carbon input into the ocean-atmosphere system ranges from 177 \pm 1 Pg C in LGMatmctl to 198 \pm 1 Pg C in LGMatmpi simulations. These simulated values are slightly lower than the lower bound of the observational estimate of 511 \pm 289 Pg C, which is based on δ ¹³C measurements from benthic foraminifera (Peterson et al., 2014).

Some earlier experiments using Earth system models were able to generate a larger decline in the pCO₂ (Ödalen et al., 2020; Vollmer et al., 2022; Matsumoto et al., 2020a, b). However, these model experiments only consider the increase in atmospheric Fe deposition but not the decline in the supply from the sediment, which was included in our *-LGMallbgc conditions. When considering only the effects of Fe deposition, the average pCO₂ in the LGMatmctl-LGMFedep simulations is 63 ppm lower than in PIctl-PIallbgc, i.e., 20 ppm more than for LGMatmctl-LGMallbgc. Further, different parameter combinations also affect the changes in pCO₂, e.g., the maximum pCO₂ drawdown in LGMatmctl-LGMFedep is 75 ppm, which is close to the observations. It is worthwhile to mention that increased Fe deposition alone reduces atmospheric pCO₂ by 22.7 ppm from PIctl-PIallbgc to





PIctl-LGMFedep, which is close to the change (22.8 ppm) in another independent model experiment considering only LGM dust deposition under pre-industrial climate conditions (Nickelsen and Oschlies, 2015).

The effects of variable stoichiometry on atmospheric pCO₂ changes during the LGM have been examined in several previous studies. These include an empirical relationship between pC:P and ambient PO₄³⁻, and between pC:N and ambient NO₃⁻ (Galbraith and Martiny, 2015), as well as a power law formulation for pC:P and pC:N that considers the influences of ambient PO₄³⁻ and NO₃⁻, temperature, and light intensity (Matsumoto et al., 2020a). For models that adopt the empirical relationship between pC:P and ambient PO₄³⁻, the decline in pCO₂ increases by 13 – 16 ppm (Ödalen et al., 2020; Fillman et al., 2023). When the relationship between pC:N and ambient NO₃⁻ is also considered, the increase reaches 11 ppm (Matsumoto et al., 2020a). The power-law formulation of Matsumoto et al. (2020a) leads to an additional drawdown of 20 ppm. To compare with these findings, we calculate the changes in pC:N (26%) and pC:P (28%) from PIctl-PIallbgc to LGMatmctl-LGMFedep configuration in our simulations. Multiplying relative changes by the total pCO₂ decline gives an estimated additional drawdown of approximately 16 – 17 ppm attributable to variable stoichiometry. While this simple calculation neglects spatial variations, it provides a first-order estimate of the impact of stoichiometric flexibility on atmospheric pCO₂ drawdown, showing that the effects of changes in elemental ratios on pCO₂ in our simulations agree with previous studies considering the effects of Fe deposition.

In our experiments, pC:N and pC:P are lower under full LGM conditions (LGMatmctl-LGMallbgc) by $-0.7 \,\mathrm{mol\,mol^{-1}}$ (-8%) and $-14 \,\mathrm{mol\,mol^{-1}}$ (-10%), respectively, than in PIctl-PIallbgc. In LGMatmctl-LGMallbgc, the higher surface nutrient concentrations, resulting from the weaker biological utilisation due to a lower global temperature and reduced Fe supply from the sediment, largely influenced the elemental ratios of POM, as shown in the *-LGMFesed simulations. Nevertheless, the lower pC:N and pC:P could be simply linked to extra N and P incorporated into the POM, and do not necessarily indicate the effects of variable stoichiometry of POM on the changes in atmospheric pCO₂ is reversed in the LGMatmctl-LGMallbgc.

4.5 Effects of parameter variations

480

485

490

495

The changes in Fe supply greatly affect the mean changes in the tracers and fluxes when compared with the pre-industrial simulations, and also contribute to higher variability among the 20 simulations with different parameter settings for each model configuration (Fig. 7 and 8). It is not surprising that the variations among the 20 ensemble members are often stronger when the median values deviate more from the pre-industrial simulations, but that is not always the case. For example, NO_3^- shows a different behaviour. When compared with *-Plallbgc, the deviation of the median is highest in *-LGMFesed but the variation is much larger in *-LGMFedep (Fig. 7c). That is because the NO_3^- level is affected by N_2 fixation, WC and benthic denitrification, and the shut-down of WC denitrification in *-LGMFesed subdues the variations in NO_3^- .

Compared to the pre-industrial reference condition (PIctl-PIallbgc), atmospheric pCO₂ under full LGM conditions (LGMatmctl-LGMallbgc) decreases by 36 to 58 ppm among the 20 simulations. The difference between the minimum and maximum pCO₂ changes amounts to 50 % of the 43.5 ppm average decrease. We apply the lm (fitting linear model) function in R package "stats" to calculate P-values for the correlations between changes in pCO₂ from PIctl-PIallbgc to LGMatmctl-LGMallbgc (Δ pCO₂) and in the perturbed parameters to better understand how individual parameters contribute to the pCO₂ variation (P < 0.05,



505

515

520

525



Fig. 10). Among the 19 parameters, the nitrogen subsistence quota $(Q_{0, \text{phy}}^{\text{N}})$, temperature-dependent mortality $(\lambda_{0, \text{phy}})$, and zooplankton maximum specific ingestion rate (g_{max}) are significantly associated with the ΔpCO_2 (Fig. 10b, e, and m). Thus, not only phytoplankton- but also zooplankton (top-down)-related parameters affect the variations in pCO₂ in our simulations.

Overall, the selected 20 parameter sets yield strongly different biogeochemical fluxes, inventories, and atmospheric pCO₂ in our various LGM model configurations. The variation in the difference with pre-industrial conditions (PIctl, PIallbgc, and PIctl-PIallbgc) among the 20 simulations in each configuration originates from the different sensitivity of our model to these parameters in each model configuration. Interestingly, the ΔpCO_2 appears unrelated to cost values (Fig. 10t). Indeed, the ΔpCO_2 is not necessarily correlated with cost values, which may be explained by different correlations (a) among parameters within the best 20 parameter sets, (b) between parameters and cost values, and (c) between parameters and ΔpCO_2 . This is easiest to see when a pair of parameters is highly correlated, which means that their effects on the cost values are strongly associated. For example, $\nu_{\rm det}$ and $w_{\rm dd}$ are the strongest positively-correlated pair among the 19 parameters (Fig. S2), and because changes in $\nu_{\rm det}$ and $w_{\rm dd}$ have opposite effects on ΔpCO_2 (Fig. 10), they tend to compensate each other's effect on ΔpCO₂ in the LGMatmctl-LGMallbgc simulations. Thus, the pairs in the best 20 parameter sets yield limited changes in the ΔpCO_2 , and a strong deviation in the ΔpCO_2 can only occur when ν_{det} and w_{dd} change in opposite directions (Fig. 11a). The other case would be α_{dia} and $Q_{0,\text{phy}}^{\text{N}}$, which is the strongest negatively-correlated pair among the 19 parameters (Fig. S2). Since changes in $\alpha_{\rm dia}$ and $Q_{0, \, \rm phy}^{\rm N}$ also have opposite effects on the $\Delta {\rm pCO_2}$, changes in $\alpha_{\rm dia}$ and $Q_{0, \, \rm phy}^{\rm N}$ could result in a larger deviation in the ΔpCO_2 but the effects on the cost values remains limited (Fig. 11b), owing to a weak correlation of either parameter with the cost value among the best 20 simulations. The weak relationship between the ΔpCO_2 and cost values demonstrates the complexity of LGM model simulations with respect to the parameter settings, and emphasises the importance of perturbed parameter ensemble simulations.

5 Conclusion and Future Directions

We investigate the role of several physical and biogeochemical boundary conditions in the face of parameter uncertainty in an Earth system model for simulating marine biogeochemistry and atmospheric pCO₂ under pre-industrial and LGM conditions. We find that persistent changes in Fe supply are the most critical factor, while changes in major nutrients (NO_3^- or PO_4^{3-}) alone have limited effects, at least partly due to co-limitation effects and the variable stoichiometry of POM in the model. The results from simulations with different combinations of physical and biogeochemical boundary conditions show that physical boundary conditions also affect marine biogeochemical cycles and atmospheric pCO₂, and the variable pP:C and pN:C can contribute about 16-17 ppm additional drawdown of pCO₂ when considering LGM Fe deposition alone.

Due to the decline in sedimentary Fe input, surface NO_3^- and PO_4^{3-} are higher in the LGM than the pre-industrial simulations. This mechanism is often ignored in LGM modelling studies. Nevertheless, we show that it could have great impact on marine biogeochemical cycles, elemental ratios of POM, and the changes in the pCO₂. This Fe source to the ocean thus requires further understanding and examination.





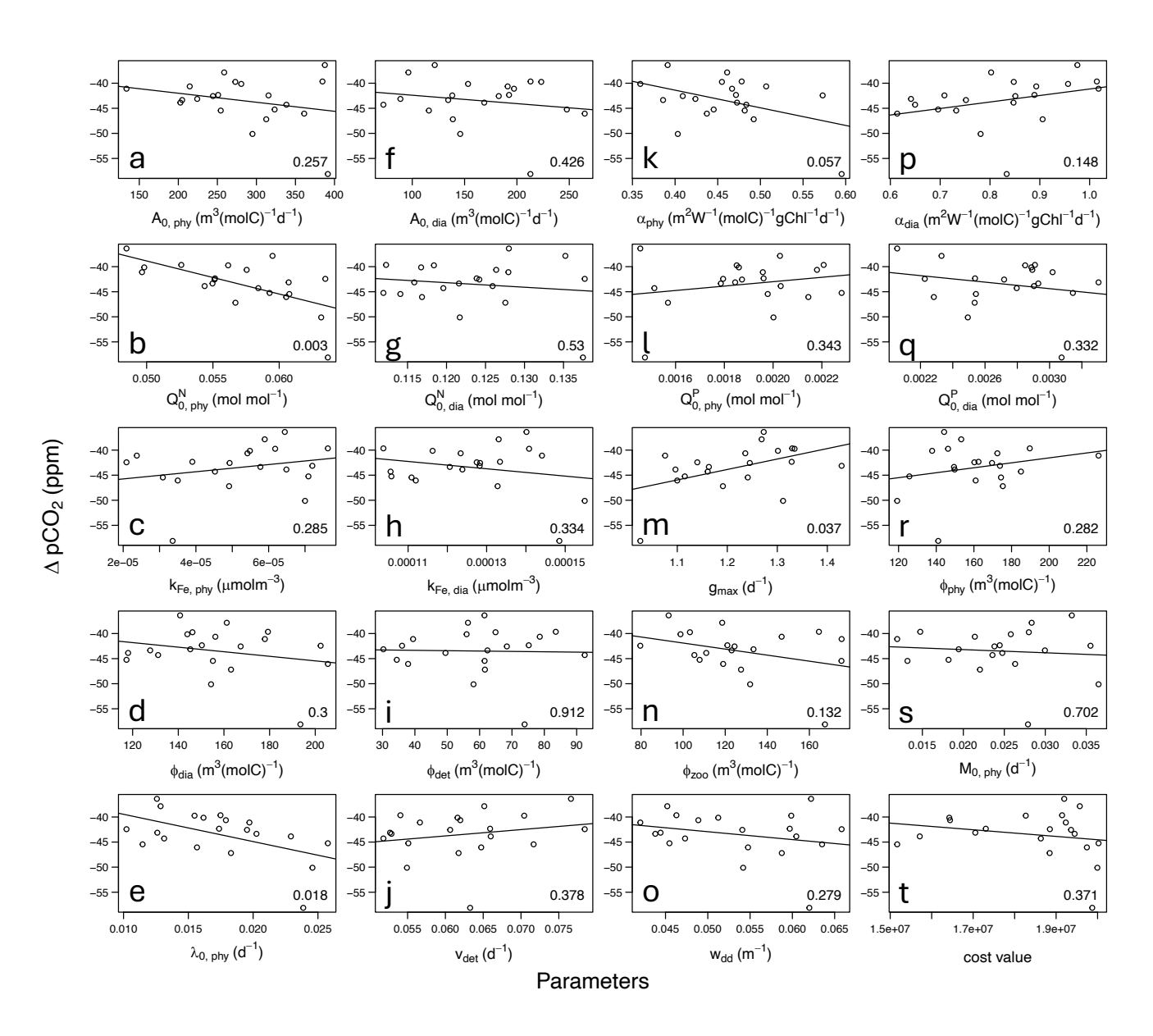


Figure 10. Changes in atmospheric pCO₂ from PIctl-PIallbgc to LGMatmctl-LGMallbgc in the 20 simulations with different parameter settings. P values are listed inside each panel.



530



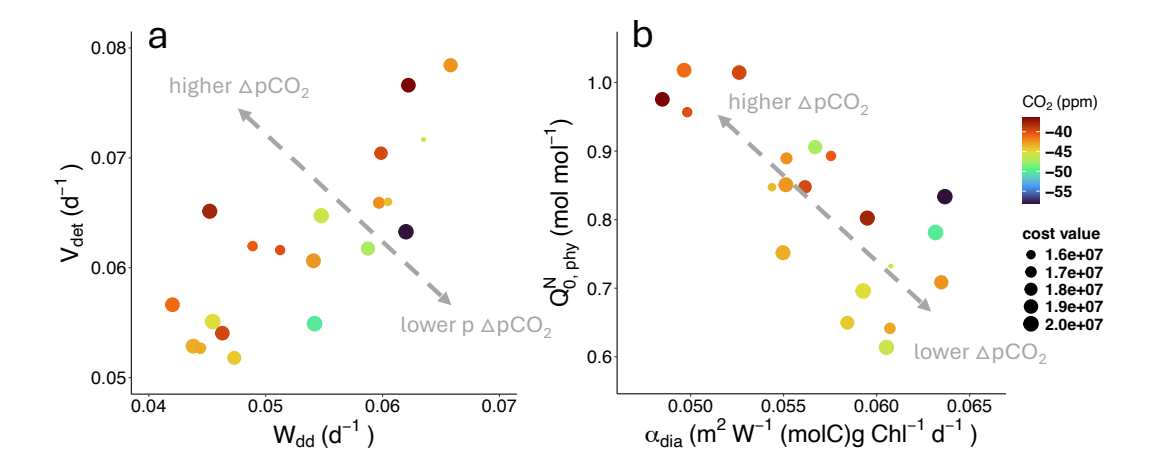


Figure 11. Effects of parameter pairs on the Δ pCO₂ between PIctl-PIallbgc and LGMatmctl-LGMallbgc. (a) ν_{det} and w_{dd} and (b) α_{dia} and $Q_{0,\text{phy}}^{\text{N}}$ are the most positively and negatively correlated pairs in the 19 parameters, respectively.

The variation of pCO₂ changes among the 20 LGM simulations highlights the uncertainty when applying parameter sets calibrated using pre-industrial conditions. We argue that understanding the uncertainty introduced by different boundary conditions and parameter sets is critical for accurately simulating LGM pCO₂ dynamics and the interactions between physical and biogeochemical factors in Earth system models.

Code availability. All model codes and data used for the analyses are available at https://doi.org/10.5281/zenodo.16630196 (Chien, 2025). All observational data in the study are publicly available, including the World Ocean Atlas 2013 (www.ncei.noaa.gov/products/ocean-climate-laboratory), GLODAPv2 (https://glodap.info/) and POM (Tanioka et al., 2022).

Author contributions. CTC designed the study, performed the model simulations, conducted the analyses, and wrote the original draft. MP contributed to the development and implementation of the optimality-based plankton ecosystem model (OPEM) and provided guidance on model configuration and interpretation. CJS assisted in the design of the glacial boundary conditions. MS contributed to the parameter calibration framework and uncertainty analysis. AO contributed to the interpretation of the results, and assisted in manuscript revision. All authors discussed the results and contributed to improving the final manuscript.

540 Competing interests. The authors declare that they have no competing interest.





Acknowledgements. Chia-Te Chien is supported by Taiwan NSTC grants NSTC 114-2611-M-002-007 -. The authors want to acknowledge use of the Ferret program of NOAA's Pacific Marine Environmental Laboratory for analysis and graphics featured in this paper.





References

- Albani, S., Mahowald, N. M., Perry, A. T., Scanza, R. A., Zender, C. S., Heavens, N. G., Maggi, V., Kok, J. F., and Otto-Bliesner, B. L.:

 Improved dust representation in the Community Atmosphere Model, Journal of Advances in Modeling Earth Systems, 6, 541–570, https://doi.org/10.1002/2013MS000279, 2014.
 - Anderson, R. F., Sachs, J. P., Fleisher, M. Q., Allen, K. A., Yu, J., Koutavas, A., and Jaccard, S. L.: Deep-Sea Oxygen Depletion and Ocean Carbon Sequestration During the Last Ice Age, Global Biogeochemical Cycles, 33, 301–317, https://doi.org/10.1029/2018GB006049, 2019.
- Bopp, L., Kohfeld, K. E., Le Quéré, C., and Aumont, O.: Dust impact on marine biota and atmospheric CO2 during glacial periods, Paleo-ceanography, 18, https://doi.org/10.1029/2002PA000810, 2003.
 - Bopp, L., Resplandy, L., Untersee, A., Le Mezo, P., and Kageyama, M.: Ocean (de)oxygenation from the Last Glacial Maximum to the twenty-first century: insights from Earth System models, Philosophical Transactions of the Royal Society A: Mathematical, Physical and Engineering Sciences, 375, 20160 323, https://doi.org/10.1098/rsta.2016.0323, 2017.
- Bouttes, N., Paillard, D., Roche, D. M., Brovkin, V., and Bopp, L.: Last Glacial Maximum CO2 and *delta*13C successfully reconciled, Geophysical Research Letters, 38, https://doi.org/10.1029/2010GL044499, 2011.
 - Broecker, W. S.: Glacial to interglacial changes in ocean chemistry, Progress in Oceanography, 11, 151 197, https://doi.org/10.1016/0079-6611(82)90007-6, 1982.
 - Brovkin, V., Ganopolski, A., Archer, D., and Rahmstorf, S.: Lowering of glacial atmospheric CO2 in response to changes in oceanic circulation and marine biogeochemistry, Paleoceanography, 22, https://doi.org/10.1029/2006PA001380, 2007.
 - Browning, T. J. and Moore, C. M.: Global analysis of ocean phytoplankton nutrient limitation reveals high prevalence of co-limitation, Nature Communications, 14, 5014, https://doi.org/10.1038/s41467-023-40774-0, 2023.
 - Browning, T. J., Achterberg, E. P., Rapp, I., Engel, A., Bertrand, E. M., Tagliabue, A., and Moore, C. M.: Nutrient co-limitation at the boundary of an oceanic gyre, Nature, 551, 242 EP –, 2017.
- Buitenhuis, E. T., Hashioka, T., and Quéré, C. L.: Combined constraints on global ocean primary production using observations and models, Global Biogeochemical Cycles, 27, 847–858, https://doi.org/10.1002/gbc.20074, 2013.
 - Carr, M.-E., Friedrichs, M. A., Schmeltz, M., Aita, M. N., Antoine, D., Arrigo, K. R., Asanuma, I., Aumont, O., Barber, R., Behrenfeld, M., Bidigare, R., Buitenhuis, E. T., Campbell, J., Ciotti, A., Dierssen, H., Dowell, M., Dunne, J., Esaias, W., Gentili, B., Gregg, W., Groom, S., Hoepffner, N., Ishizaka, J., Kameda, T., Quere, C. L., Lohrenz, S., Marra, J., Melin, F., Moore, K., Morel, A., Reddy, T. E., Ryan, J., Scardi,
- 570 M., Smyth, T., Turpie, K., Tilstone, G., Waters, K., and Yamanaka, Y.: A comparison of global estimates of marine primary production from ocean color, Deep Sea Research Part II: Topical Studies in Oceanography, 53, 741 770, https://doi.org/10.1016/j.dsr2.2006.01.028, 2006.
 - Chien, C.-T.: Code and data for: Chien et al., Ensemble simulation of the Last Glacial Maximum marine biogeochemistry and atmospheric pCO2 drawdown due to the soft-tissue biological carbon pump, https://doi.org/10.5281/zenodo.16630196, 2025.
- 575 Chien, C.-T., Pahlow, M., Schartau, M., and Oschlies, A.: Optimality-based non-Redfield plankton–ecosystem model (OPEM v1.1) in UVic-ESCM 2.9 Part 2: Sensitivity analysis and model calibration, Geoscientific Model Development, 13, 4691–4712, https://doi.org/10.5194/gmd-13-4691-2020, 2020.
 - Chien, C.-T., Pahlow, M., Schartau, M., Li, N., and Oschlies, A.: Effects of phytoplankton physiology on global ocean biogeochemistry and climate, Science Advances, 9, eadg1725, https://doi.org/10.1126/sciadv.adg1725, 2023.





- Deutsch, C., Sigman, D. M., Thunell, R. C., Meckler, A. N., and Haug, G. H.: Isotopic constraints on glacial/interglacial changes in the oceanic nitrogen budget, Global Biogeochemical Cycles, 18, https://doi.org/10.1029/2003GB002189, 2004.
 - Eugster, O., Gruber, N., Deutsch, C., Jaccard, S. L., and Payne, M. R.: The dynamics of the marine nitrogen cycle across the last deglaciation, Paleoceanography, 28, 116–129, https://doi.org/10.1002/palo.20020, 2013.
- Fay, A. R. and McKinley, G. A.: Global open-ocean biomes: mean and temporal variability, Earth Syst. Sci. Data, 6, 273–284, https://doi.org/10.5194/essd-6-273-2014, 2014.
 - Fillman, N., Schmittner, A., and Kvale, K. F.: Variable Stoichiometry Effects on Glacial/Interglacial Ocean Model Biogeochemical Cycles and Carbon Storage, https://doi.org/10.22541/essoar.169049091.16856096/v1, 2023.
 - Galbraith, E. D. and Martiny, A. C.: A simple nutrient-dependence mechanism for predicting the stoichiometry of marine ecosystems, Proceedings of the National Academy of Sciences, 112, 8199–8204, https://doi.org/10.1073/pnas.1423917112, 2015.
- Garcia, H. E., Locarnini, R. A., Boyer, T. P., Antonov, J. I., Mishonov, A. V., Baranova, O. K., Zweng, M. M., Reagan, J. R., and Johnson, D. R.: Dissolved Oxygen, Apparent Oxygen Utilization, and Oxygen Saturation, in: World Ocean Atlas 2013, edited by Levitus, S., vol. 3, NOAA Atlas NESDIS 75, http://www.nodc.noaa.gov/OC5/indprod.html, 2013a.
 - Garcia, H. E., Locarnini, R. A., Boyer, T. P., Antonov, J. I., Mishonov, A. V., Baranova, O. K., Zweng, M. M., Reagan, J. R., and Johnson, D. R.: Dissolved Inorganic Nutrients (phosphate, nitrate, silicate), in: World Ocean Atlas 2013, edited by Levitus, S., vol. 4, NOAA Atlas NESDIS 76, http://www.nodc.noaa.gov/OC5/indprod.html, 2013b.
 - Glock, N., Erdem, Z., Wallmann, K., Somes, C. J., Liebetrau, V., Schönfeld, J., Gorb, S., and Eisenhauer, A.: Coupling of oceanic carbon and nitrogen facilitates spatially resolved quantitative reconstruction of nitrate inventories, Nature Communications, 9, 1217, https://doi.org/10.1038/s41467-018-03647-5, 2018.
- Gruber, N. and Sarmiento, J. L.: Global patterns of marine nitrogen fixation and denitrification, Global Biogeochemical Cycles, 11, 235–266, https://doi.org/10.1029/97GB00077, 1997.
 - Honjo, S., Manganini, S. J., Krishfield, R. A., and Francois, R.: Particulate organic carbon fluxes to the ocean interior and factors controlling the biological pump: A synthesis of global sediment trap programs since 1983, Progress in Oceanography, 76, 217 285, https://doi.org/10.1016/j.pocean.2007.11.003, 2008.
- Huang, Y., Tagliabue, A., and Cassar, N.: Data-Driven Modeling of Dissolved Iron in the Global Ocean, Frontiers in Marine Science, 9, https://doi.org/10.3389/fmars.2022.837183, 2022.
 - Isles, P. D. F.: The misuse of ratios in ecological stoichiometry, Ecology, 101, e03 153, https://doi.org/10.1002/ecy.3153, 2020.
 - Jaccard, S. L. and Galbraith, E. D.: Large climate-driven changes of oceanic oxygen concentrations during the last deglaciation, Nature Geoscience, 5, 151–156, https://doi.org/10.1038/ngeo1352, 2012.
- Jacobel, A., Anderson, R., Jaccard, S., McManus, J., Pavia, F., and Winckler, G.: Deep Pacific storage of respired carbon during the last ice age: Perspectives from bottom water oxygen reconstructions, Quaternary Science Reviews, 230, 106065, https://doi.org/10.1016/j.quascirev.2019.106065, 2020.
 - Jolliff, J. K., Kindle, J. C., Shulman, I., Penta, B., Friedrichs, M. A., Helber, R., and Arnone, R. A.: Summary diagrams for coupled hydrodynamic-ecosystem model skill assessment, Journal of Marine Systems, 76, 64 82, https://doi.org/10.1016/j.jmarsys.2008.05.014, skill assessment for coupled biological/physical models of marine systems, 2009.
- Kageyama, M., Harrison, S. P., Kapsch, M.-L., Lofverstrom, M., Lora, J. M., Mikolajewicz, U., Sherriff-Tadano, S., Vadsaria, T., Abe-Ouchi, A., Bouttes, N., Chandan, D., Gregoire, L. J., Ivanovic, R. F., Izumi, K., LeGrande, A. N., Lhardy, F., Lohmann, G., Morozova, P. A., Ohgaito, R., Paul, A., Peltier, W. R., Poulsen, C. J., Quiquet, A., Roche, D. M., Shi, X., Tierney, J. E., Valdes, P. J., Volodin, E., and Zhu,



625

645



- J.: The PMIP4 Last Glacial Maximum experiments: preliminary results and comparison with the PMIP3 simulations, Climate of the Past, 17, 1065–1089, https://doi.org/10.5194/cp-17-1065-2021, 2021.
- Kemppinen, K. M. S., Holden, P. B., Edwards, N. R., Ridgwell, A., and Friend, A. D.: Coupled climate–carbon cycle simulation of the Last Glacial Maximum atmospheric CO₂ decrease using a large ensemble of modern plausible parameter sets, Climate of the Past, 15, 1039–1062, https://doi.org/10.5194/cp-15-1039-2019, 2019.
 - Key, R. M., Olsen, A., van Heuven, S., Lauvset, S. K., Velo, A., Lin, X., Schirnick, C., Kozyr, A., Tanhua, T., Hoppema, M., Jutterström, S., Steinfeldt, R., Jeansson, E., Ishii, M., Perez, F. F., and Suzuki, T.: Global Ocean Data Analysis Project, Version 2 (GLODAPv2), https://doi.org/10.3334/CDIAC/OTG.NDP093_GLODAPv2, 2015.
 - Khatiwala, S., Schmittner, A., and Muglia, J.: Air-sea disequilibrium enhances ocean carbon storage during glacial periods, Science Advances, 5, eaaw4981, https://doi.org/10.1126/sciadv.aaw4981, 2019.
 - Kobayashi, H., Oka, A., Yamamoto, A., and Abe-Ouchi, A.: Glacial carbon cycle changes by Southern Ocean processes with sedimentary amplification, Science Advances, 7, eabg7723, https://doi.org/10.1126/sciadv.abg7723, 2021.
- Kriest, I., Kähler, P., Koeve, W., Kvale, K., Sauerland, V., and Oschlies, A.: One size fits all? Calibrating an ocean biogeochemistry model for different circulations, Biogeosciences, 17, 3057–3082, https://doi.org/10.5194/bg-17-3057-2020, 2020.
 - Lauvset, S. K., Key, R. M., Olsen, A., van Heuven, S., Velo, A., Lin, X., Schirnick, C., Kozyr, A., Tanhua, T., Hoppema, M., Jutterström, S., Steinfeldt, R., Jeansson, E., Ishii, M., Perez, F. F., Suzuki, T., and Watelet, S.: A new global interior ocean mapped climatology: GLODAP version 2, Earth System Science Data, 8, 325–340, https://doi.org/10.5194/essd-8-325-2016, 2016.
- 635 Li, N., Somes, C. J., Landolfi, A., Chien, C.-T., Pahlow, M., and Oschlies, A.: Global impact of benthic denitrification on marine N₂ fixation and primary production simulated by a variable-stoichiometry Earth system model, Biogeosciences, 21, 4361–4380, https://doi.org/10.5194/bg-21-4361-2024, 2024.
 - Martin, J. H.: Glacial-interglacial CO2 change: The Iron Hypothesis, Paleoceanography, 5, 1–13, https://doi.org/https://doi.org/10.1029/PA005i001p00001, 1990.
- Martin, J. H., Knauer, G. A., Karl, D. M., and Broenkow, W. W.: VERTEX: carbon cycling in the northeast Pacific, Deep Sea Research Part A. Oceanographic Research Papers, 34, 267 285, https://doi.org/10.1016/0198-0149(87)90086-0, 1987.
 - Martínez-García, A., Sigman, D. M., Ren, H., Anderson, R. F., Straub, M., Hodell, D. A., Jaccard, S. L., Eglinton, T. I., and Haug, G. H.: Iron Fertilization of the Subantarctic Ocean During the Last Ice Age, Science, 343, 1347, https://doi.org/10.1126/science.1246848, 2014.
 - Matsumoto, K., Rickaby, R., and Tanioka, T.: Carbon Export Buffering and CO2 Drawdown by Flexible Phytoplankton C:N:P Under Glacial Conditions, Paleoceanography and Paleoclimatology, 35, e2019PA003 823, https://doi.org/10.1029/2019PA003823, 2020a.
 - Matsumoto, K., Tanioka, T., and Rickaby, R.: Linkages Between Dynamic Phytoplankton C:N:P and the Ocean Carbon Cycle Under Climate Change, Oceanography, 33, 44–52, https://doi.org/10.5670/oceanog.2020.203, 2020b.
 - McCarthy, G., Smeed, D., Johns, W., Frajka-Williams, E., Moat, B., Rayner, D., Baringer, M., Meinen, C., Collins, J., and Bryden, H.: Measuring the Atlantic Meridional Overturning Circulation at 26°N, Progress in Oceanography, 130, 91–111, https://doi.org/10.1016/j.pocean.2014.10.006, 2015.
 - McElroy, M. B.: Marine biological controls on atmospheric CO2 and climate, Nature, 302, 328–329, https://doi.org/10.1038/302328a0, 1983. Mengis, N., Keller, D. P., MacDougall, A. H., Eby, M., Wright, N., Meissner, K. J., Oschlies, A., Schmittner, A., MacIsaac, A. J., Matthews, H. D., and Zickfeld, K.: Evaluation of the University of Victoria Earth System Climate Model version 2.10 (UVic ESCM 2.10), Geoscientific Model Development, 13, 4183–4204, https://doi.org/10.5194/gmd-13-4183-2020, 2020.





- Mills, M. M., Brown, Z. W., Lowry, K. E., van Dijken, G. L., Becker, S., Pal, S., Benitez-Nelson, C. R., Downer, M. M., Strong, A. L., Swift, J. H., Pickart, R. S., and Arrigo, K. R.: Impacts of low phytoplankton NO3:PO4 utilization ratios over the Chukchi Shelf, Arctic Ocean, Deep Sea Research Part II: Topical Studies in Oceanography, 118, 105–121, https://doi.org/10.1016/j.dsr2.2015.02.007, more from NASA's ICESCAPE (Impacts of Climate on EcoSystems and Chemistry of the Arctic Pacific Environment) program, Part 1, 2015.
- Muglia, J. and Schmittner, A.: Glacial Atlantic overturning increased by wind stress in climate models, Geophysical Research Letters, 42, 9862–9868, https://doi.org/10.1002/2015GL064583, 2015.
 - Muglia, J., Somes, C. J., Nickelsen, L., and Schmittner, A.: Combined Effects of Atmospheric and Seafloor Iron Fluxes to the Glacial Ocean, Paleoceanography, 32, 1204–1218, https://doi.org/10.1002/2016PA003077, 2017.
 - Nickelsen, L. and Oschlies, A.: Enhanced sensitivity of oceanic CO2 uptake to dust deposition by iron-light colimitation, Geophysical Research Letters, 42, 492–499, https://doi.org/10.1002/2014GL062969, 2015.
- Ödalen, M., Nycander, J., Ridgwell, A., Oliver, K. I. C., Peterson, C. D., and Nilsson, J.: Variable C/P composition of organic production and its effect on ocean carbon storage in glacial-like model simulations, Biogeosciences, 17, 2219–2244, https://doi.org/10.5194/bg-17-2219-2020, 2020.
 - Pahlow, M., Chien, C.-T., Arteaga, L. A., and Oschlies, A.: Optimality-based non-Redfield plankton–ecosystem model (OPEM v1.1) in UVic-ESCM 2.9 Part 1: Implementation and model behaviour, Geoscientific Model Development, 13, 4663–4690, https://doi.org/10.5194/gmd-13-4663-2020, 2020.
 - Peterson, C. D., Lisiecki, L. E., and Stern, J. V.: Deglacial whole-ocean δ^{13} C change estimated from 480 benthic foraminiferal records, Paleoceanography, 29, 549–563, https://doi.org/10.1002/2013PA002552, 2014.
 - Saini, H., Meissner, K. J., Menviel, L., and Kvale, K.: Impact of iron fertilisation on atmospheric CO₂ during the last glaciation, Climate of the Past, 19, 1559–1584, https://doi.org/10.5194/cp-19-1559-2023, 2023.
- Sarmiento, J. L. and Toggweiler, J. R.: A new model for the role of the oceans in determining atmospheric P CO2, Nature, 308, 621–624, https://doi.org/10.1038/308621a0, 1984.
 - Schartau, M., Wallhead, P., Hemmings, J., Löptien, U., Kriest, I., Krishna, S., Ward, B. A., Slawig, T., and Oschlies, A.: Reviews and syntheses: parameter identification in marine planktonic ecosystem modelling, Biogeosciences, 14, 1647–1701, https://doi.org/10.5194/bg-14-1647-2017, 2017.
- Séférian, R., Gehlen, M., Bopp, L., Resplandy, L., Orr, J. C., Marti, O., Dunne, J. P., Christian, J. R., Doney, S. C., Ilyina, T., Lindsay, K., Halloran, P. R., Heinze, C., Segschneider, J., Tjiputra, J., Aumont, O., and Romanou, A.: Inconsistent strategies to spin up models in CMIP5: implications for ocean biogeochemical model performance assessment, Geoscientific Model Development, 9, 1827–1851, https://doi.org/10.5194/gmd-9-1827-2016, 2016.
- Shao, Z., Xu, Y., Wang, H., Luo, W., Wang, L., Huang, Y., Agawin, N. S. R., Ahmed, A., Benavides, M., Bentzon-Tilia, M., Berman-Frank,
 I., Berthelot, H., Biegala, I. C., Bif, M. B., Bode, A., Bonnet, S., Bronk, D. A., Brown, M. V., Campbell, L., Capone, D. G., Carpenter,
 E. J., Cassar, N., Chang, B. X., Chappell, D., Chen, Y.-L., Church, M. J., Cornejo-Castillo, F. M., Detoni, A. M. S., Doney, S. C., Dupouy,
 C., Estrada, M., Fernandez, C., Fernández-Castro, B., Fonseca-Batista, D., Foster, R. A., Furuya, K., Garcia, N., Goto, K., Gago, J.,
 Gradoville, M. R., Hamersley, M. R., Henke, B. A., Hörstmann, C., Jayakumar, A., Jiang, Z., Kao, S.-J., Karl, D. M., Kittu, L. R., Knapp,
 A. N., Kumar, S., LaRoche, J., Liu, H., Liu, J., Lory, C., Löscher, C. R., Marañón, E., Messer, L. F., Mills, M. M., Mohr, W., Moisander,
- P. H., Mahaffey, C., Moore, R., Mouriño Carballido, B., Mulholland, M. R., Nakaoka, S., Needoba, J. A., Raes, E. J., Rahav, E., Ramírez-Cárdenas, T., Reeder, C. F., Riemann, L., Riou, V., Robidart, J. C., Sarma, V. V. S. S., Sato, T., Saxena, H., Selden, C., Seymour, J. R., Shi, D., Shiozaki, T., Singh, A., Sipler, R. E., Sun, J., Suzuki, K., Takahashi, K., Tan, Y., Tang, W., Tremblay, J.-E., Turk-Kubo, K., Wen, Z.,





- White, A. E., Wilson, S. T., Yoshida, T., Zehr, J. P., Zhang, R., Zhang, Y., and Luo, Y.-W.: Global oceanic diazotroph database version 2 and elevated estimate of global oceanic N₂ fixation, Earth System Science Data, 15, 3673–3709, https://doi.org/10.5194/essd-15-3673-2023, 2023.
- Sigman, D. M., De Boer, A. M., and Haug, G. H.: Antarctic Stratification, Atmospheric Water Vapor, and Heinrich Events: a Hypothesis for Late Pleistocene Deglaciations, pp. 335–349, American Geophysical Union (AGU), ISBN 9781118666241, https://doi.org/https://doi.org/10.1029/173GM21, 2007.
- Somes, C. J., Schmittner, A., Muglia, J., and Oschlies, A.: A Three-Dimensional Model of the Marine Nitrogen Cycle during the Last Glacial Maximum Constrained by Sedimentary Isotopes, Frontiers in Marine Science, 4, 108, https://doi.org/10.3389/fmars.2017.00108, 2017.
 - Somes, C. J., Dale, A. W., Wallmann, K., Scholz, F., Yao, W., Oschlies, A., Muglia, J., Schmittner, A., and Achterberg, E. P.: Constraining Global Marine Iron Sources and Ligand-Mediated Scavenging Fluxes With GEOTRACES Dissolved Iron Measurements in an Ocean Biogeochemical Model, Global Biogeochemical Cycles, 35, e2021GB006948, https://doi.org/10.1029/2021GB006948, 2021.
- Tagliabue, A., Bopp, L., Roche, D. M., Bouttes, N., Dutay, J.-C., Alkama, R., Kageyama, M., Michel, E., and Paillard, D.: Quantifying the roles of ocean circulation and biogeochemistry in governing ocean carbon-13 and atmospheric carbon dioxide at the last glacial maximum, Climate of the Past, 5, 695–706, https://doi.org/10.5194/cp-5-695-2009, 2009.
 - Tagliabue, A., Bopp, L., Dutay, J.-C., Bowie, A. R., Chever, F., Jean-Baptiste, P., Bucciarelli, E., Lannuzel, D., Remenyi, T., Sarthou, G., Aumont, O., Gehlen, M., and Jeandel, C.: Hydrothermal contribution to the oceanic dissolved iron inventory, Nature Geoscience, 3, 252–256, https://doi.org/10.1038/ngeo818, 2010.
- Tagliabue, A., Aumont, O., DeAth, R., Dunne, J. P., Dutkiewicz, S., Galbraith, E., Misumi, K., Moore, J. K., Ridgwell, A., Sherman, E., Stock, C., Vichi, M., Völker, C., and Yool, A.: How well do global ocean biogeochemistry models simulate dissolved iron distributions?, Global Biogeochemical Cycles, 30, 149–174, https://doi.org/10.1002/2015GB005289, 2016.
 - Tanioka, T., Garcia, C. A., Larkin, A. A., Garcia, N. S., Fagan, A. J., and Martiny, A. C.: Global patterns and predictors of C:N:P in marine ecosystems, Communications Earth & Environment, 3, 271, https://doi.org/10.1038/s43247-022-00603-6, 2022.
- Vollmer, T. D., Ito, T., and Lynch-Stieglitz, J.: Proxy-Based Preformed Phosphate Estimates Point to Increased Biological Pump Efficiency as Primary Cause of Last Glacial Maximum CO2 Drawdown, Paleoceanography and Paleoclimatology, 37, e2021PA004339, https://doi.org/10.1029/2021PA004339, 2022.
 - Wallmann, K.: Phosphorus imbalance in the global ocean?, Global Biogeochemical Cycles, 24, https://doi.org/10.1029/2009GB003643, 2010.
- Wallmann, K., Schneider, B., and Sarnthein, M.: Effects of eustatic sea-level change, ocean dynamics, and nutrient utilization on atmospheric pCO₂ and seawater composition over the last 130 000 years: a model study, Climate of the Past, 12, 339–375, https://doi.org/10.5194/cp-12-339-2016, 2016.
 - Wang, W.-L., Moore, J. K., Martiny, A. C., and Primeau, F. W.: Convergent estimates of marine nitrogen fixation, Nature, 566, 205–211, https://doi.org/10.1038/s41586-019-0911-2, 2019.